CHALMERS
UNIVERSITY OF TECHNOLOGY

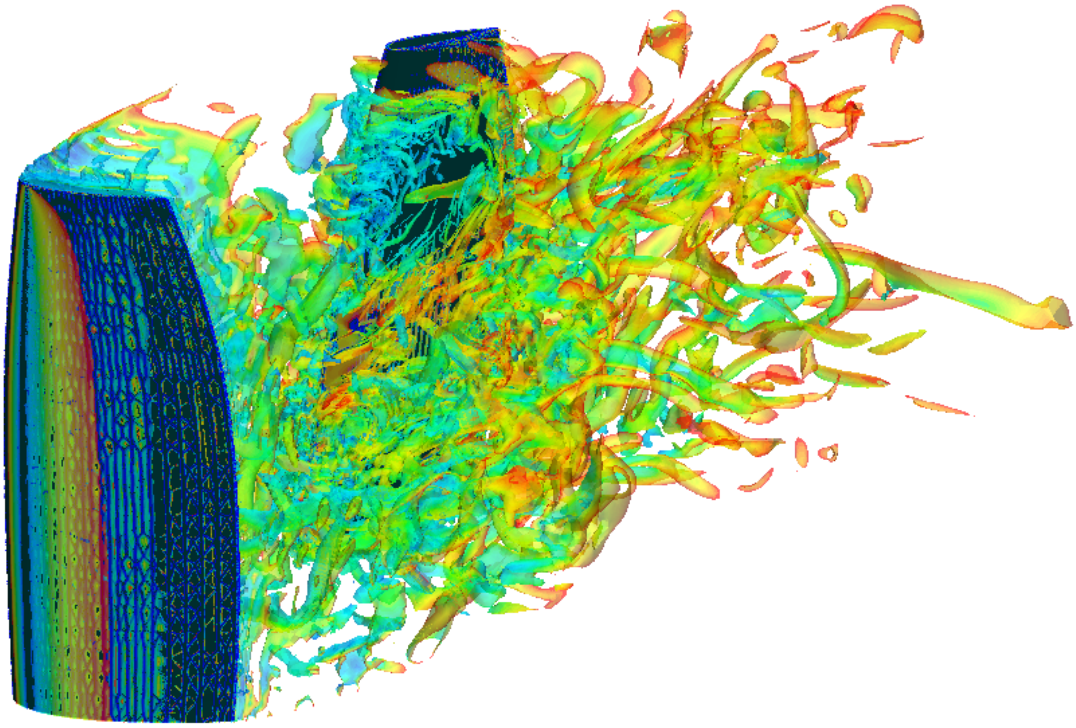

CFD investigation of wind powered ships under extreme conditions

Master's thesis in Naval Architecture and Ocean Engineering

Henry Blount
Jose Maria Portell

DEPARTMENT OF MECHANICS AND MARITIME SCIENCES

CHALMERS UNIVERSITY OF TECHNOLOGY
Gothenburg, Sweden 2021
www.chalmers.se

Master's thesis 2021

CFD investigation of wind powered ships under extreme conditions

Climate change is making humans re-think the way of transporting by using non-pollutant energies. Wind propulsion is a promising alternative. This report investigates the aerodynamic behaviour of a sail for wind-powered ships under different wind conditions by using CFD.

HENRY BLOUNT
JOSE MARIA PORTELL

Department of Mechanics and Maritime Sciences
Division of Marine Technology
Chalmers University of Technology
Gothenburg, Sweden 2021

CFD investigation of wind powered ships under extreme conditions
HENRY BLOUNT
JOSE MARIA PORTELL

Supervisors: Laura Marimon Giovannetti, SSPA; Da-Qing Li, SSPA
Examiner: Rickard Bensow, Department of Mechanics and Maritime Sciences

Report number: 2021:75

Master's Thesis 2021
Department of Mechanics and Maritime Sciences
Division of Marine Technology

Chalmers University of Technology
SE-412 96 Gothenburg
Telephone +46 31 772 1000

Cover: Velocity visualization created in Star CCM+ showing an ISO surface with a Q-criteron of $1250/s^2$.

Typeset in LaTeX
Printed by Chalmers Reproservice
Gothenburg, Sweden 2021

CFD investigation of wind powered ships under extreme conditions
Henry Blount
Jose Maria Portell
Department of Mechanics and Maritime Sciences
Chalmers University of Technology

Abstract

With the International Maritime Organization's (IMO) goal of reducing greenhouse gas emissions 50% by 2050, the design and propulsion of ships must change rapidly. The use of wind propulsion is one solution. A CFD analysis has been performed using the sail geometry of the Oceanbird Ro-Ro ship, with the purpose of determining the forces on the sails.

Star-CCM+ has been used to analyze the NACA 0015 wing profile in both 2D and 3D. In 2D, the $k - \omega$ SST model has been employed to compare the lift and drag coefficients with wind tunnel data and to show the effects of dynamic stall. In 3D, the IDDES model has been used to compute the lift and drag coefficients with 3D effects and to determine the interaction effects between multiple wings

CFD results show that lift and drag forces slightly differ from the forces seen in previous wind tunnel experiments. The physical time plays an important role in the simulations, both in the 2D and 3D situations, what has led to different conclusions, mainly in relation to the setup of the mesh and physics of the investigation. Dynamic stall affects the performance of the wing when rotating from one angle of attack to another, being the biggest determinant the rotational speed. Both the integrity of the structure and the thrust production need to be considered when establishing the dynamic stall situation. In the multiple wing simulations, the rear wing has shown to be severely affected by the leading wing during stalled conditions. Finally, the frequencies of vibrations from vortex shedding have been calculated which are interesting for the structural integrity of the rig, concluding that the stalled situations should be avoided since the shedding frequencies could compromise the structure.

Suggestions for further work include wind tunnel tests to confirm the data in this report and a more in-depth structural analysis.

Keywords: CFD, Oceanbird, Naval Architecture, NACA0015, Windship, Sailing, Shipping, Climate Change.

Acknowledgements

This master thesis has been conducted as the final work of the Master's in Naval Architecture and Ocean Engineering at the Department of Mechanics and Maritime Sciences, at Chalmers University of Technology. This work has been done by Jose Maria Portell and Henry Blount.

We would like to thank first Laura Marimon Giovannetti and Da-Qing Li for guiding us through the project as our supervisors of the thesis. They have answered all of our questions and have given us their feedback and thoughts on any matter related to the thesis in the shortest possible time. Although they were not initially assigned to this project, we really appreciate their help and commitment since the very beginning of the investigations and thank them for this. Further, thanks to Laura, we were able to speak directly to Ciro Cannavacciuolo, a Siemens Support expert, who helped us several times with the software and the thesis.

Our examiner, Rickard Bensow, has also been essential in the execution of the thesis, giving us his feedback and extensive knowledge in the subject studied. We would like to thank him too for his guidance and help along the project.

Karolina Malmek has also been key to encouraging us to carry out this project. She helped us in previous coursework and guided us through the initial stages of this thesis.

Also, thanks to Rolf Sörmans fund, we were able to visit the KTH's installations, where the Oceanbird's model scale is tested. Thanks to the fund, we were able to see with our own eyes the extent of the project by meeting people involved in different areas of this big project. Among others, we had the chance of meeting Ulysse Dhome, who is in charge of these tests and showed us how everything related to the model performance. It was an honour to represent Chalmers and Rolf Sörmans foundation in Stockholm.

Finally, we would like to thank both SSPA and Wallenius Marine for giving us the opportunity to be a part of this incredible project. We have enjoyed every single moment of the work, which would not be possible without them.

Jose Maria Portell and Henry Blount, Gothenburg, August, 2021.

Contents

List of Figures

List of Tables

Acronyms

JAMDA	Japanese Marine Machinery Development Association
NACA	National Advisory Committee for Aeronautics
IMO	International Maritime Organization
CFD	Computational Fluid Dynamics
DES	Detached Eddy Simulation
IDDES	Improved Delayed Detached Eddy Simulation
SNIC	Swedish National Infrastructure for Computing
C3SE	Chalmers Centre for Computational Science and Engineering
AR	aspect ratio
LEV	leading-edge vortex
FV	Finite Volume
FE	Finite Element
RANS	Reynolds Averaged Navier Stokes
uRANS	unsteady Reynolds Averaged Navier Stokes
FFT	Fast Fourier Transform
DFT	Discrete Fourier Transformation
AoA	angle of attack
LES	Large Eddy Simulation
DNS	Direct Numerical Simulation
CL	coefficient of lift
CD	coefficient of drag
TS	Time-Step
Re	Reynolds Number
GHG	Greenhouse Gases
SST	Shear Stress Transport
CFL	Courant-Friedrichs-Lewy
CPU	Central Processing Unit

1

Introduction

This project focuses on investigating extreme conditions that wind powered ships could encounter, when the wings have large angles of attack and the flow becomes stalled. A stalled condition is reached when the flow separates from the airfoil and does not re-attach [5]. This situation could also lead to large unsteady forces, harming the integrity of the whole ship. To investigate these conditions, different CFD analysis are carried out by using the computational tool STAR CCM+. Moreover, several methods are studied to develop the simulations and predict the loading condition on a NACA-0015 airfoil.

In an early basis, the flow is studied in a 2D simulation for one wing to see where and when the flow starts to detach from the foil and thus, find the worst possible scenarios. Moreover, this case gives the opportunity of comparing the results obtained with experimental data from other available researches. Once this is performed, the 3D simulation is developed to simulate the real sailing condition, analyse the adverse situations and develop scenarios for wind tunnel tests. Finally, the forces and vibrations involved are also studied. After finishing the one wing simulation, the same procedure is used to investigate the interaction of multiple wings. This simulation gives the most real possible solution.

1.1 A brief history of sailing

The use of wind as a means of propulsion in shipping is not a new concept. The earliest known evidence of sailing ships is from 2000 BC in Egypt [7]. These boats featured a single square sail for propulsion, a rig that existed until the Roman times [7]. The first known depiction of a sailboat was painted on a Gerzean era jar, shown in Figure 1.1 [1].

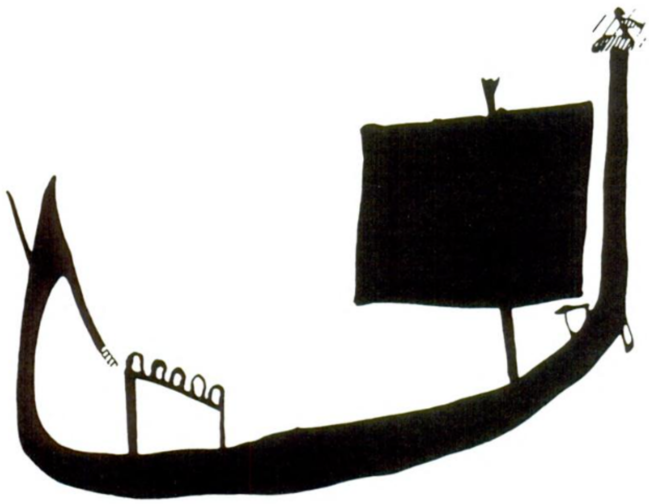

Figure 1.1: The first known image of a sailboat [1]

Many other civilizations developed sailing ships in the early years, including: the Vikings, the Romans and the Chinese. Development of sailing ships accelerated between the fifteenth and seventeenth centuries, with the advent of the fully rigged ship [8]. This is the era when sailing ships began to have more than one mast. Development of merchant sailing ships continued until the end of the clipper ship era from 1845-1875 [9].

The switch away from sailing ships was accelerated by the opening of the Suez Canal. The Suez Canal enabled steamers to make the journey to the far-east. It reduced the distance by half and there were several locations along the route where the ship could be refueled [10]. The switch to steam occurred rapidly. By 1870 UK shipbuilders started to produce more steam ships than sailing ships [10]. Sailing ships still had their role in transporting certain low value cargoes like grain on long distance routes such as the Australia to UK route. Sail remained the dominant shipping method through the early turn of the 20th century on some routes [11]. The sailing trade continued to diminish, until 1949 when the German ship Pamir became the last commercial sailing ship to round Cape Horn [12]. Since then the sailing ship has not returned to commercial success. There was renewed interest in wind propulsion during the 1970s oil crisis [13]. The Japanese Marine Machinery Development Association (JAMDA) created around 10 different wind assisted ships in the 1980s [13]. Wind ships have continued to be researched but have not been met with commercial success. However, many new companies have been investing in this topic in recent years.

1.2 Background

With the rise in global temperatures due to climate change, the shipping industry must act to reduce harmful levels of pollution being emitted. The International Maritime Organization (IMO) represents the United Nations' specialized agency with responsibility for the prevention of marine and atmospheric pollution by ships. The agency has set CO_2 reduction targets for global shipping, with the goal of reducing greenhouse gas emissions by 50% by 2050 when compared with 2008 Greenhouse Gases (GHG) emission levels. In April 2018, the IMO adopted the 'Initial IMO Strategy on Reduction of GHG Emissions for Ships', the initial contribution to the global goals defined in the Paris Agreement to maintain the the global average temperature below 2 deg C above pre-industrial levels. To fully achieve this goal more needs to be done than simply switching to a less harmful fuel source. Sails have the opportunity to significantly reduce the GHG emissions from shipping.

The Oceanbird is a joint project carried out by Wallenius Marine, KTH Royal Institute of Technology and SSPA. The goal for the ship is to carry 7000 cars across the Atlantic Ocean at 10 knots with a transit time of 12 days. This will all be accomplished with a 90% reduction in GHG emissions compared with a diesel engine. This is achieved with the use of 5 telescopic wing sails for the majority of the propulsion.

1.3 IT tools

1.3.1 Computational Fluid Dynamics

Computational Fluid Dynamics (CFD) is a way of analyzing fluid flow problems. All CFD solvers have three main parts: a pre-processor, a solver, and a post-processor. The pre-processor is involved with setting up the physics conditions, definition of the boundaries, fluid properties and the mesh. The solver performs the calculations by applying the governing equations in an iterative manner over each cell of the mesh. The post-processor takes the resulting data and displays it in graphs or figures that make it easier for the user to analyze.

At best, the CFD software will replicate the physics of the problem [14]. But this accurate representation can be affected by both the mesh setup and the modelling. In general, a finer mesh will produce more accurate results, but this is at the expense of computational time. The trade off between accuracy and computational time make the mesh development key in any CFD simulation. The model also effects the results. In general, RANS is a good model and is used widely in CFD simulations. However, in situations with large areas of separation it is better to use another model. In this case the DES model is used.

1.3.2 Star-CCM+

For this project the CFD software Star-CCM+[15] is being used. Star-CCM+ is a commercial CFD software that is developed by Siemens. The software uses a finite volume method to solve the Navier-Stokes equation over the entire mesh. Star-CCM+ has built in physics models such as $k-\omega$ and Detached Eddy Simulation (DES) that make it a very useful package for this project.

1.3.3 Vera cluster

In this thesis the computer cluster Vera was used for all simulations. Vera is a Chalmers resource with additional help provided by Chalmers Centre for Computational Science and Engineering (C3SE). Access to this resource was essential for completing this project.

2

Theory

2.1 Theory definition

In order to understand the main physics behind sailing, this chapter reviews the different aerodynamic terms as well as the forces that appear on the foil when a flow interacts with it.

2.1.1 Aerodynamic forces

The geometry of the cross-section of the foil can be described in four main terms: leading edge, trailing edge and chord length and thickness. The leading edge is the foremost part of the wing which has the maximum curvature, the trailing edge is the aft part of the airfoil, the chord line is the straight line connecting the leading and trailing edge, while the thickness varies along the foil and can be measured either perpendicular to the chamber line or to the chord line [2].

Also, the body can be divided into two main different areas: suction and pressure surface. The first one, also called upper surface, is associated with the higher velocity and lower pressure, while the pressure surface, or lower surface, has the opposite behavior.

An airfoil subjected to a flow, creates an aerodynamic force due to the relative motion between the body and the gas. This force arises from two causes:

- The normal force due to the pressure on the surface of the body
- The shear force due to the viscosity of the gas (i.e. skin friction).

The total aerodynamic force equals to both normal and shear forces integrated over the foil's exposed area. When this airfoil is moving relatively to the air, the aerodynamic force appears in the backward direction and with an angle dependent on the direction of the relative motion. This force can be decomposed into two, lift and drag forces, which through the body's center of pressure.

- Drag force acts parallel to the direction of the relative motion
- Lift force acts perpendicular to the direction of the relative motion

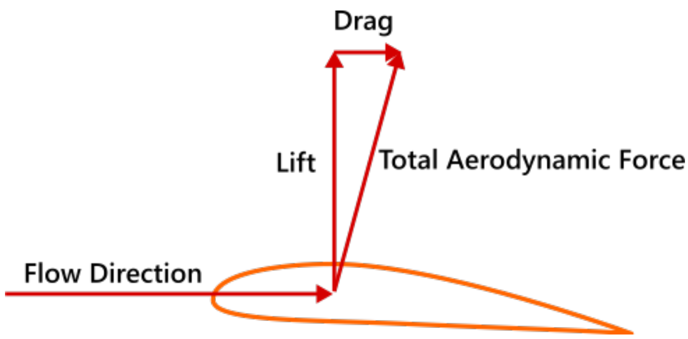

Figure 2.1: Aerodynamic forces [2]

In order to be able to compare the calculations with experimental data, non-dimensional coefficients are introduced. In the case of the lift, the coefficient expression is described as:

$$C_L = \frac{2F_L}{\rho U_2 A} \tag{2.1}$$

Where F_L is the lift force, rho is the density, U the velocity and A the area of the body.
The drag coefficient is presented as:

$$C_L = \frac{2F_D}{\rho U_2 A} \tag{2.2}$$

Where F_D is the drag force.

In this project, the pressure coefficient is also used to study the behavior of the flow around the foil, which is described next.

$$C_P = \frac{p - p_\infty}{0.5\rho V_\infty^2} \tag{2.3}$$

Where p is the static pressure where the pressure coefficient is evaluated, p_∞ is the static pressure in the free stream, rho is the fluid density and V_∞ is the velocity of the flow.

2.1.2 NACA0015

National Advisory Committee for Aeronautics (NACA) are airfoil shapes for aircraft and other structures wings. The shape of these airfoils is described by a series of digits which can be entered into equations to generate the cross-section of the wing and calculate the properties.

Lift and drag coefficients help to understand the behavior of a wing under different circumstances of speed and direction of the wind. As presented in previous chapters, the Oceanbird's wing profile has a NACA0015-like shape, where the main characteristics are its symmetry and a 15% thickness to chord length ratio [3]. Due to the need of operating with wind coming from both starboard or port side, symmetry profiles help to achieve a full performance in every side of the wing for different sailing circumstances.

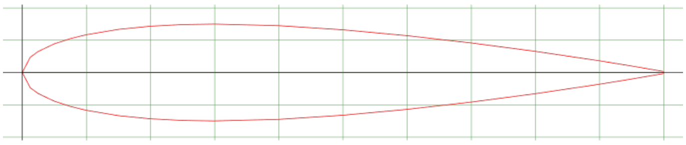

Figure 2.2: NACA0015 wing profile [3]

2.1.3 Aspect Ratio

The aspect ratio (AR) is a geometric property of an airfoil that is shown to have effects on the performance of the airfoil. It is defined as.

$$AR = \frac{S^2}{A} \tag{2.4}$$

Where S is the wing span and A is the area of the wing. The difference in aerodynamics between a high and low AR is the effect of the wingtip vortices on the lift and drag. Wingtip vortices are caused by the high pressure fluid on one side of the airfoil spilling over to the low pressure side of the airfoil, it is shown in Figure 2.3.

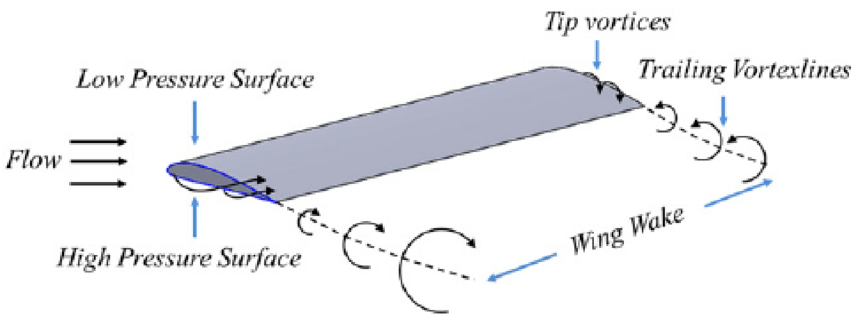

Figure 2.3: Wingtip vortices on an airfoil [4]

With a high AR airfoil the tip is usually smaller, therefore the tip vortices have less of an effect on the total area of the airfoil. The wingtip vortices are a major factor in reducing the lift coefficient on a wing this is especially true of low AR wings [16]. To account for the effects of the AR is very complex, but an equation has been formulated to capture a majority of these effects in a simple way [17].

$$C_l = \frac{C_{l0}}{1 + \frac{C_{l0}}{\pi AR}} \tag{2.5}$$

Where C_l is the final lift coefficient, C_{l0} is the freestream lift coefficient, and AR is the aspect ratio of the wing. This can be used to correct for any AR differences when comparing data.

2.1.4 Flow situations

In aerodynamics, the flow can be divided into two basic flow areas, the boundary layer region and the external flow region, which are presented in Figure 2.4.

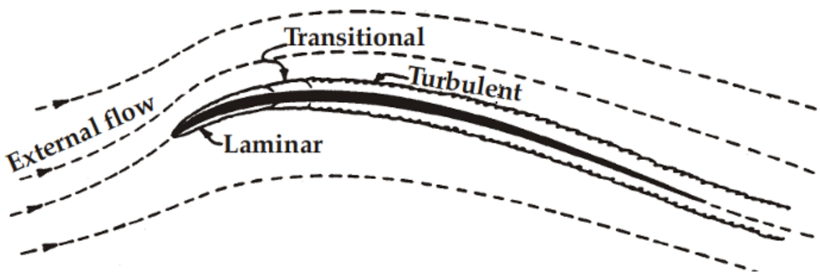

Figure 2.4: Boundary layer regions [5]

The boundary layer flow region represents the layer of air that is very close to the region. Because of the viscosity of the flowing gas, in this case air, the particles that touch the airfoil have zero speed with respect to the surface of the foil and are carried out along by the wing. The air close to the surface moves with a finite velocity while the air at the edge of the boundary layer moves with the speed of the boundary layer. The second flow area, external flow region, corresponds to the airflow and does not affect to the aerodynamic calculations regarding the viscosity.

Deeper into the boundary layer, it is also divided into three types. The laminar boundary layer appears in the leading edge of an airfoil and it is characterized for having a very smooth change of airspeed. In this situation, the lift coefficient is very high compared to the drag. When the unsteadiness within the boundary layer starts to develop, as well as disturbances due to, for example, a change of the angle of attack, the smooth changes turn into more erratic flows, leading to a short transitional boundary layer. When the unsteadiness and disturbances get even greater, the flow becomes turbulent. In this case, the skin friction drag gets greater compared to the laminar situation.

A stall condition corresponds to a reduction in the lift coefficient when the angle of attack increases. This situation appears when the critical angle of attack of the wing is surpassed. This critical point depends mainly on the fluid and Reynolds number. In case of the NACA0015, this angle is between 17 and 18 degrees [18].

The Reynolds number is the ratio of the inertial forces to the viscous forces. When the Reynolds number is high it indicates that the inertial forces dominate and after a certain point can be considered inviscid. While low Reynolds numbers indicate that the viscous forces play a significant part in the flow characteristics. The Reynolds Number (Re) is a similarity parameter for the viscous forces and in general dictates the flow velocity in CFD. It creates similar conditions for similar problems so that results can easily be compared. It is defined by the following equation

$$Re = \frac{\rho V L}{\mu} \tag{2.6}$$

where: ρ is the fluid density, V is the fluid velocity, L is the length, and μ is the bulk viscosity.

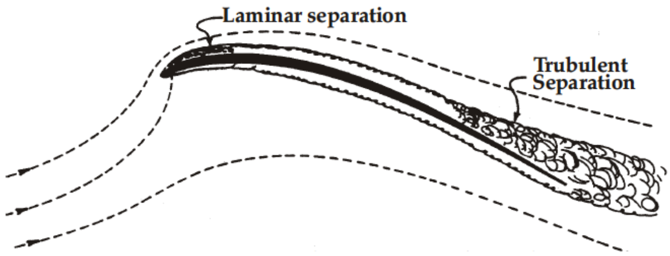

Figure 2.5: Aerodynamic separation types [5]

It is also important to highlight that the airflow can be either attached or separated to the wing. With low angle of attacks, the air flows attached along the foil but, when this angle is increased, the boundary layer does no longer follow the surface, appearing a separation of the flow. The separation occurs when the external pressure in the surface increases too rapidly. Then, depending on the rate of change of pressure, the separation can be laminar or turbulent.

2.1.5 Dynamic Stall

As observed earlier, drag coefficient affects negatively to the performance of the sail. The higher this coefficient is, the less thrust the wing provides. Then, it is desirable to have higher lift coefficients and a large difference between both aerodynamic coefficients.

Further into this, one possibility of delaying the appearance of the turbulent flow separation is dynamically pitching the foil with a certain angular speed and to a certain angle of attack. The shear layer near the leading edge rolls up to form an leading-edge vortex (LEV), providing additional suction over the upper wing surface (a-c. Figure 2.6). This additional suction leads to an increase in the lift and stall delay. This phenomenon is called dynamic stall. However, the LEV situation becomes rapidly unstable, detaching the flow from the foil (d-f. Figure 2.6). The drag increases as well as the pitching moment, what can lead to violent vibrations and high loads, thus fatigue and structural damage [19].

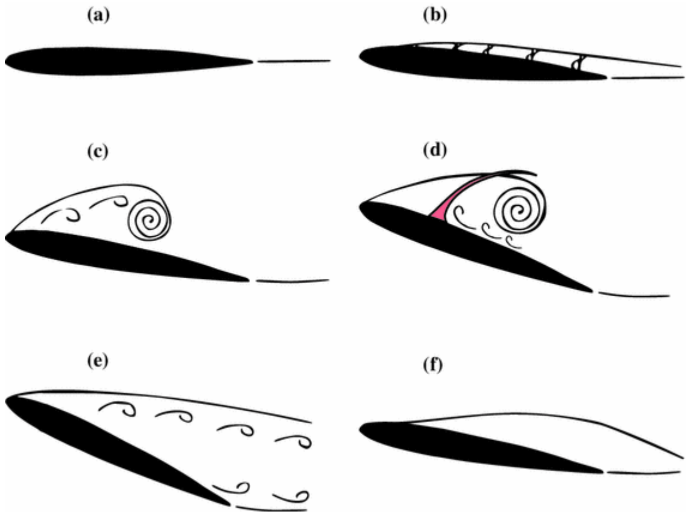

Figure 2.6: Dynamic stall effect [6]

The rotational speed to create the dynamic stall condition depends, among other parameters, on the reduced frequency. This frequency is dimensionless and defines the degree of unsteadiness of the problem. Further, the reduced frequency can be used to explain the variation of the lift and drag coefficients when the amplitude is attenuated and the phase is lag [20]. The reduced frequency is defined as the following expression.

$$k = \frac{\omega b}{V} \tag{2.7}$$

where k is the reduced frequency, ω is the angular velocity, b is the airfoil's chord length and V is the flow velocity. Based on the value of the reduced frequency, it can divide the flow into:

- Steady state aerodynamics: $k = 0$
- Quasi-steady aerodynamics: $0 \leq k \leq 0.05$
- Unsteady aerodynamics: $k > 0.05$ ($k > 0.2$ is considered highly unsteady)

2.2 Meshing

A mesh is a discretized representation of a geometric domain. The domain generally contains the study geometry, its content and its surrounding environment [21]. In the case of this project, the domain represents a wind-tunnel containing the wing that is studied. However, different setups, as it will be explained later, are performed depending on whether the investigation is in 2D or 3D.

For this investigation, the meshes are generated with Star-CCM+. Due to this, the parameters and concepts explained are related to those used by the software.

As explained earlier, the simulations are divided in two parts: 2D and 3D. The first part has been used to analyse the influence of the mesh in the solutions. For this analysis, results from both experimental and computational calculations have been compared in order to obtain an accurate and efficient mesh.

2.2.1 Star-CCM+ meshing

Simcenter Star-CCM+ provides several options for both surface and volume meshing operations. For Finite Volume (FV), the software computes values for all cell centers, while for Finite Element (FE), it is done at element nodes. In this project, different turbulence models that require volume control models are used, thus the FV approach is performed in this investigation.

2.2.2 Computational domain

The computational domain refers to the portion of space where the CFD simulation is performed. This form should contain all the physically important aspects of the problem. Then, the domain has to be discretized into a computational grid, also called mesh, to solve the discretized equations of the fluid [22] [23].

However, one critical aspect of the simulations is to evaluate the computational space. If the domain is too big, the calculations will be slow and will take computational space, but if the domain is too small, some of the important phenomena will be missed. In general, the visualization tool shows quickly and intuitively if the mesh is adequate or not [24]. Although several studies propose different rules, according to S. Leonardi and I.P. Castro [25], the domain should be at least 8 times the length of geometry studied. This is taken as a base to do the simulations needed.

2.2.3 Boundary conditions

As explained in previous sections, the boundary layer flow corresponds to the flow at the solid walls, where the fluid's velocity is equal to zero. The boundary layer refers to the transition layer between the wall and the flow. Since profiles with some angle of attack can not employ wall functions [26], the boundary layer is defined all the way to the wall with improved wall treatment by refining the mesh close to the wall. In the case of Star-CCM+, the boundary layer characteristics are defined in the so-called Prism Layer Mesher as it is explained in further sections.

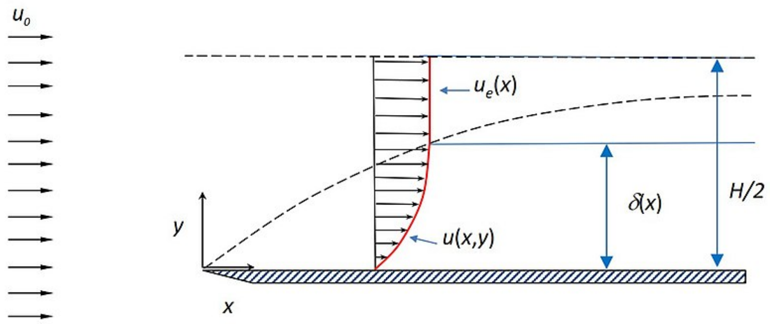

Figure 2.7: Boundary layer in a 2D plate

To resolve this boundary layer, a non-dimensional wall length parameter called $y+$ is used which describes the distance from the wall. This parameter should be no longer than 1 for the no-slip conditions so then the flow is within the viscous sublayer [27]. One of way of controlling the y+ value is controlling the near-wall thickness. This parameter is calculated as:

$$y^+ = \frac{y \rho u_*}{\mu} \tag{2.8}$$

Where y is the thickness of the first mesh cell along the wall, ρ is the fluid density, u_* is the representative value of the flow velocity in the wall region, hence the friction velocity, and μ is the dynamic viscosity of the fluid [28]. Further into this, due to the fact that a prism layer is used, the boundary layer thickness, $\sigma(x)$ in Figure 2.7, has to be calculated as well. According to the Blasius solution conditions, the layer value is closely approximated by

$$\sigma_{99}(x) = 5 \frac{x}{\sqrt{Re_x}} \tag{2.9}$$

where x is the distance from the leading edge and Re_x is the Reynolds number occurring in the x direction.

2.3 Physics Models

When using Star-CCM+ for this CFD analysis, a physics model must be selected. In this project the models that are being studied are the Reynolds Averaged Navier Stokes (RANS) model and the DES model. Both are being studied to compare the results, with the basic principles of each being described below.

2.3.1 Reynolds Averaged Navier Stokes (RANS)

The Reynolds Averaged Navier Stokes (RANS) model is a common model used in CFD today. RANS is a model that uses average values for the variables in steady state and dynamic flow fields. It also can be used with unsteady simulations when using the modified Unsteady Reynolds Averaged Navier Stokes (uRANS) model. In addition to the RANS model itself, it also needs a turbulence model to calculate the turbulent effects on the flow field. These turbulence models are explained further in the sections below.

2.3.2 $k - \omega$ SST Model

The $k - \omega$ Shear Stress Transport (SST) model is a turbulence model that is used alongside a RANS simulation within Star-CCM+. This model shares similarities to the $k - \epsilon$ model, being the main difference that the $k - \omega$ SST model uses a hybrid approach.

Far away, only the $k - \epsilon$ is used but within the boundary layer the $k - \omega$ is used. In the region adjacent to the boundary layer a combination of both approaches is used. The standard $k - \epsilon$ model is written as:

$$\frac{\partial}{\partial t}(\rho k) + \nabla \cdot (\rho U k) = \nabla \cdot ((\mu + \frac{\mu_t}{\sigma_k})\nabla k) + P_k - \rho\epsilon \tag{2.10}$$

$$\frac{\partial}{\partial t}(\rho \epsilon) + \nabla \cdot (\rho U \epsilon) = \nabla \cdot ((\mu + \frac{\mu_t}{\sigma_k})\nabla \epsilon + C_{1\epsilon} P_k \frac{\epsilon}{k} - C_{2\epsilon}\rho\frac{\epsilon^2}{k} \tag{2.11}$$

Equation 2.10 represents the kinetic energy and equation 2.11 is the dissipation equation. The difference with the $k - \omega$ model is a substitution within the dissipation equation.

$$\epsilon = C_\mu k \omega \tag{2.12}$$

If equation 2.12 is inserted into equation 2.11 we get an equation that is very similar to the $k - \omega$ model, with the exception of an additional term. Performing the substitution gives:

$$\frac{\partial}{\partial t}(\rho \omega) + \nabla \cdot (\rho U \omega) = \nabla \cdot ((\mu + \frac{\mu_t}{\sigma_k})\nabla \omega + \frac{\gamma}{\nu_t} P_k - \beta\rho\omega^2 + 2\frac{\rho\sigma_{\omega 2}}{\omega}\nabla k : \nabla\omega \tag{2.13}$$

When comparing equation 2.13 with the $k - \omega$ model one can see that the only difference is the last term. To establish the equation in the $k - \omega$ SST model the equations need to be controlled. If the additional term in equation 2.13 is multiplied by $(1 - F_1)$, it turns into a blending function that controls when $k - \omega$ or $k - \epsilon$ is used.

$$2(1 - F1)\frac{\rho\sigma_{\omega 2}}{\omega}\nabla k : \nabla\omega \tag{2.14}$$

when:

F_1=0, the model is pure $k - \epsilon$
F_1=1, the model is pure $k - \omega$

Within Star CCM+ the blending function (F_1) that is used is

$$F_1 = \tanh([\min(\max(\frac{\sqrt{k}}{0.09\omega d}, \frac{500v}{d^2\omega}), \frac{2k}{d^2 CD_{k\omega}})]^4) \tag{2.15}$$

Equation 2.15 will control how much effect either $k-\epsilon$ or $k-\omega$ have on the model. The equation depends on the distance from the wall (d). At the wall F_1 will approach 1 while far away from the wall F_1 will approach 0. In addition to blending the dissipation equation F_1 also blends together the coefficients, such as β and σ_k. A more standard way of representing the transport equations in the $k-\omega$ SST model is

$$\frac{\partial}{\partial t}(\rho k) + \nabla \cdot (\rho k \bar{v}) = \nabla \cdot [(\mu + \sigma_k \mu_t)\nabla k] + P_k - \rho\beta^* f_{\beta^*}(\omega k - \omega_0 k_0) + S_k \tag{2.16}$$

$$\frac{\partial}{\partial t}(\rho \omega) + \nabla \cdot (\rho \omega \bar{v}) = \nabla \cdot [(\mu + \sigma_\omega \mu_t)\nabla \omega] + P_\omega - \rho\beta f_\beta(\omega^2 - \omega_0^2) + S_\omega \tag{2.17}$$

2.3.3 Detached Eddy Simulation (DES)

The DES is a hybrid model that combines RANS with LES depending on the location within the mesh. RANS simulations are applied to the boundary layers, while the Large Eddy Simulation (LES) are applied in the unsteady separated regions. The integral length scale is very important in LES as the mesh requires a minimum of 4 cells to resolve an eddy.

$$l_0 = \frac{k^{1/2}}{C_\mu \omega} \tag{2.18}$$

The integral length scale is shown in equation 2.18. In an attempt to resolve much of the turbulent kinetic energy without using too much computational power, an 80-90% resolution rate is considered satisfactory. To achieve an 80% resolution rate the integral length from equation 2.18 must equal to the length of 5 cells. To get a satisfactory mesh this simulation will need to be run several times to refine the mesh in the right locations.

The standard DES model in Star-CCM+ is the Improved Delayed Detached Eddy Simulation (IDDES). For an IDDES model ω, the specific dissipation rate, is replaced in equation 2.16. It is replaced with a new value of $\tilde{\omega}$.

$$\tilde{\omega} = \frac{\sqrt{k}}{l_{hybrid} f_{\beta^*} \beta^*} \tag{2.19}$$

2.3.4 Transition Models

The transition model is applied to the turbulent kinetic energy equation shown in equation 2.13 through the γ term. It controls the production of turbulent kinetic energy. That term represents the intermittency of the transition. A value of 1 indicates a fully turbulent flow, where 100% of the domain is turbulent. Conversely, a value of 0 indicates a fully laminar flow where turbulence does not exist within the domain. Within Star-CCM+ there are several transition models available. The two that are of most interest are the Gamma Transition and the Gamma ReTheta Transition. They are both solve the intermittency transport equation.

$$\frac{d}{dt}(\rho\gamma) + \nabla \cdot (\rho\gamma\bar{v}) = \nabla \cdot [(\mu + \frac{\mu_t}{\sigma_f})\nabla\gamma] + P_\gamma - E_\gamma \tag{2.20}$$

where ρ is the density, $\bar{v}$ is the mean velocity, μ is the dynamic viscosity, μ_t is the turbulent eddy viscosity, σ_f is the model coefficient, P_γ is the production term, and E_γ is the destruction term.

The difference between the Gamma Transition and the Gamma ReTheta Transition lays in the production and destruction coefficients: σ_f, P_γ, and E_γ. The Gamma ReTheta Transition model solves for two additional transport equations in addition to the two-equation SST K-Omega model. In contrast, the Gamma Transition model only solves for one equation—it is therefore faster and less computationally expensive than the Gamma ReTheta Transition model [21].

2.3.5 Courant Number

In order to accurately capture the time dependent flow simulation, the Courant Number needs to be set to a value less than 1.

$$CFL = \frac{U\Delta T}{\Delta x} \tag{2.21}$$

where U is the free stream velocity, ΔT is the time step, and Δx is the length of the cell.

This constraint needs to be satisfied because otherwise the fluid particle could be lost within the domain. A Courant Number of less than one physically represents that one fluid particle cannot move through more than one cell during one time step. Since Δx is set during the mesh process, U is known and Courant-Friedrichs-Lewy (CFL) must be less than one, the time-step is calculated from equation 2.21. Within Star-CCM+ this can be set automatically using the Convective CFL Condition. All that is needed within Star-CCM+ is a target and maximum CFL number. Once that is set an appropriate time step will be chosen within the program. The Star-CCM+ routine considers both the CFL number as well as the Von Neumann stability conditions.

2.4 Fast Fourier Transform (FFT)

A fast Fourier transform (FFT) is an algorithm that computes the discrete Fourier transform (DFT) of a sequence, or its inverse (IDFT). Fourier analysis converts a signal from its original domain (often time or space) to a representation in the frequency domain and vice versa. The DFT is obtained by decomposing a sequence of values into components of different frequencies [29]. The algorithm was developed in 1965 by James Cooley and John Turkey [30]. The Fast Fourier Transform (FFT) will show all frequencies detected in the signal and the strength of each frequency component in relation to the other components. The algorithm changes the x axis form time to frequency and decomposes the signal into it's pure frequency components. It is an optimized version of the Discrete Fourier Transformation (DFT)).

$$A_k = \sum_{n=0}^{N-1} e^{-i\frac{2\pi}{N}kn} a_n \tag{2.22}$$

The FFT is prefered over the DFT due to the speed of the computation. Going from DFT to FFT results in the computation being reduced from $O(N^2)$ to $O(Nlog_2(N))$ [31]. This becomes a massive savings in computational power when the inputs are large.

3
Methods

The aim of this project is to investigate the response of the Oceanbird's wing under different wind conditions. This wing represents a cross-sectional shape of a NACA0015 airfoil. In order to verify the values obtained with CFD in Star-CCM+, the results have always been compared with the experimental data obtained by Sandia National Laboratories regarding the lift and drag coefficients [32].

The data from the Sandia National Laboratory was tested at Wichita State University in a wind tunnel with dimensions of 7 feet (2.134 m) by 10 feet (3.048 m). During testing, the wind tunnel was fitted with inserts to simulate two-dimensional conditions. The 2-D test section becomes 3 feet (0.914 m) wide by 7 feet (2.134 m) tall with the inserts in place. The airfoils were then mounted to both inserts. The airfoil was rotated from a 0 to 180 degree angle of attack. The control mechanism to control the angle of attack only had a range of 60 degrees, so the model had to be re-mounted three times to get the full range of motion. The airfoils were designed to be aerodynamically smooth and had a chord length of 6 inches (15.24 cm) in length. The tests were run at several Reynolds numbers, one of which matches the Reynolds number in this investigation. With this data, the CFD investigation could be checked and confirm that the simulations were properly executed.

The comparison with Heng Zhu's work [33] is to compare the results between CFD simulations. Zhu used the software OpenFOAM which is interesting to be compared with this project's STAR-CCM+ investigations. Any effects due to the solver will hopefully be shown with this comparison.

The project is divided into two parts- 2D and 3D simulations. The first part investigates the effect of the mesh in the solutions, as well as the dynamic stall condition. In the case of the 3D, the simulations cover the problems relates to structure forces and vibrations, together with the interaction of multiple wings.

3.1 Geometry

The geometry that is used in this project has been provided by SSPA. This geometry represents the Oceanbird's wing in real scale, as seen in Figure 3.1.

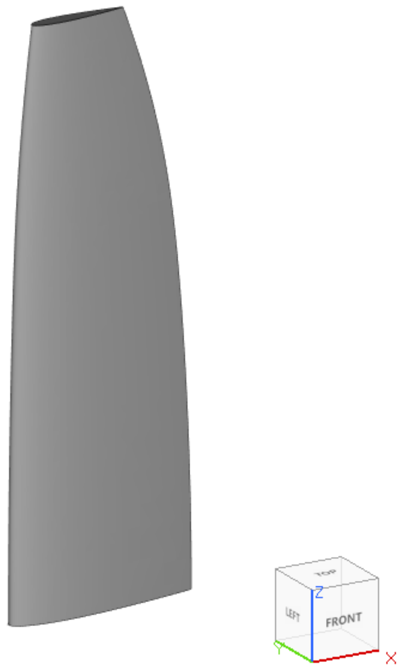

Figure 3.1: 3D wing provided by SSPA

The dimensions of the wing are 26.6 meters of chord length, 80 meters high and 4 meters wide. However, working with a full scale takes computational time and storage space. For this reason, the wing is scaled down to a chord length of 1 meter. Further, this scaling allows to compare the results with the experimental data. Sandia [32] used airfoils with chord lengths of one meter.

Although the wing has different chord lengths along the height, the wing profile used in the 2D simulations has also a chord length of 1m to be compared with the experimental data.

With the geometry and in order to execute the simulations, the domain has to be defined first. The domain represents the wind tunnel where the wing is exposed to the conditions of the investigation. For this reason, the domain design (Figure 3.2) should be big enough to capture accurately the response of the foil to these conditions.

Figure 3.2: Wind-tunnel domain

The body is created in the 3D-CAD extension of Star-CCM+. This parametric solid modeller dispose of multiple features and tools that allows to create simple geometries. The domain is then created complying the conditions defined in the section 2.2.2. Due to the fact that the domain has to capture the wake of the airfoil, the length of the body has been greatly increased. Also, as it will be presented in the next section, one of the investigations performed aims to study the effect of the flow direction with respect to the foil and the cells of the mesh. For this reason, the inlet part of the domain is set to have a "C-shape".

With this, two different domains have been created, one for each study part. In the 2D case, the domain has a width of 8 meters and 30 meters of length. For the 3D case, the domain is 40 meters long, 16 meters wide and 15 meters tall.

3.2 2D simulations

This section aims to briefly explain the configuration of the mesh in 2D with which the simulations have been performed. As explained earlier, the 2D mesh is also used in the 3D simulations to create the grid. However, the first unknown that appears is whether the flow direction or the airfoil direction should change for different angles of attack, the purpose of this investigation is to analyse the angles of attack from 0 to 180 degrees. Once this is solved, a physics analysis is performed to see the behaviour of different solvers in the software. as well as a brief discussion of the Courant number analysis. Last, a comparison between a fixed mesh and an overset mesh is done to finally obtain the drag and lift coefficients that are used for the present investigation.

3.2.1 Mesh setup

The main purpose of analysing the mesh in 2D is to make a faster and more efficient study of the influence of the setup in terms of results accuracy, computational time and storage. 2D meshes require a fewer number of cells than 3D since the geometry is simplified. For this reason, the analysis and conclusions carried out in this section will directly be used in the 3D case.

Star-CCM+ enables choosing different mesh types related to the shape of the cells and meshing procedure. With the domain defined, the mesh needs to be created to calculate the conditions of the investigation. In this project, the automated mesh is generated with trimmed cells. Trimmed Mesher uses by default a template mesh that is composed by hexahedral cells at the target size with trimmed cells next to the surface [21]. Further, to improve the overall quality of the mesh surface, the Surface Remesher is employed, which is also used to optimize the mesh for the volume mesh models.

Close to the foil is where the flow is disturbed, then, refinement in this region is needed. The Prism Layer Mesher performs this refinement, which generates orthogonal prismatic cells next to the wall surfaces and boundaries. This layer helps the solver to resolve the flow near the wall accurately, which is vital to determine forces or other flow features, such as separation. Moreover, using a prism layer mesh allows to solve the viscous sublayer directly if the turbulence model support it, thus having a low $y+$ (~ 1) in the wall treatment. Typically, the number of cells in the cross-stream direction oscillates between 10-20 cells [21]. In this project, the number of prism layer is set to 20.

Despite the Prism Layer Mesher, more refinement is needed to capture the reaction of the flow when hitting the airfoil. A new refinement region is created to solve this problem with a rectangular shape, which has a length 9 times the foil chord length and a height of 4 times the foil.

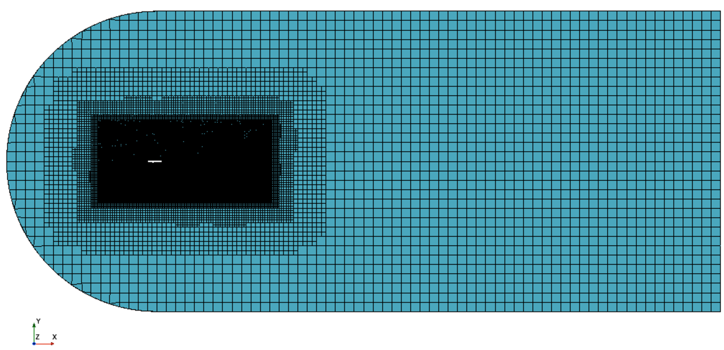

Figure 3.3: Mesh in 2D in the whole domain

The resulting mesh is shown in Figure 3.3. The base cell element is 0.5 meters to reduce the computational time and the storage space. Since the interest regions are around the airfoil, the refinement area decreases the size of the cell down to 0.05 meters. The transition from the base cell elements to the refinement region has to be as smooth as possible, ideally having an aspect ratio close to the unit to ensure that quantities such as the momentum are transferred appropriately throughout the system [24]. The Surface Growth Rate is set to 1.2 so then 4 different sizes appear between these two regions.

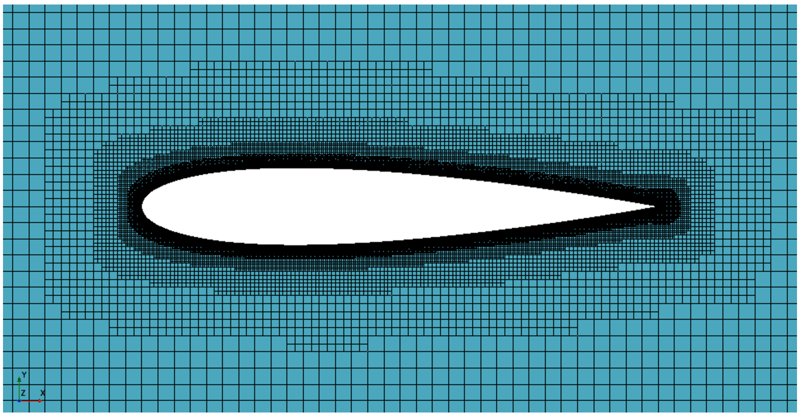

Figure 3.4: 2D mesh in the refinement region around the airfoil

More in detail into the refinement region, the Prism Layer Mesher is set to have a thickness of 7.5e-3 meters composed by 20 layers. Following section 2.2.3, the prism layer surpasses by 5e-3 meters the thickness needed, what makes an extra refinement, thus a more accurate resolution. Last, also following the section just mentioned, the prism layer thickness near the wall is set to 2.3e-5 m.

With this setup, the mesh obtained has 19 million cells. Compared to similar works [34], the number of cells resembles to them. This investigation requires a precise grid to capture the behaviour of the wing in high angles of attack where the flow becomes turbulent, appearing more unsteady and uncontrolled.

3.2.2 Grid direction

The cells orientation has to be first analysed to choose whether the wing or the flow direction should change in every AoA. Star-CCM+ gives the possibility of changing the flow direction, simulating different angles of attack. However, as the direction of the fluid changes, so it does the cell alignment with respect to the flow. Also, the wind-tunnel (the domain) would no longer have a parallel orientation with respect to the flow.

According to Warey et al. [35], numerical diffusion can occur when local flow direction is not aligned with the mesh. In detail, Warey et al. [35] argues that typical numerical discretization schemes for the Navier-Stokes equations generates very accurate results when the grid is aligned with the flow direction. Further, they observe that numerical diffusion increases exponentially when the streamline direction gets over 45º with respect to the mesh. These disturbances can lead to less accurate results.

In order to check the effect of this, two simulations are run changing the flow and the airfoil direction separately in an interval of 0 to 12 degrees AoA. These results are also compared with the experimental data and the results from OpenFOAM, as seen in figures 3.5 and 3.6. The circles represent the data calculated while the lines are an interpolation of these points.

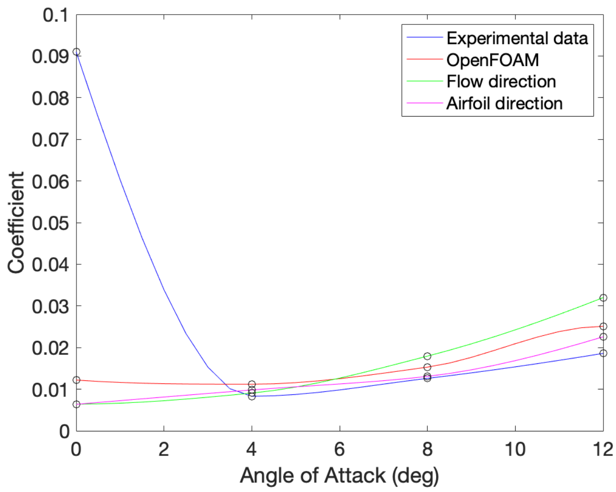

Figure 3.5: Investigation of the mesh alignment evaluating the drag coefficient

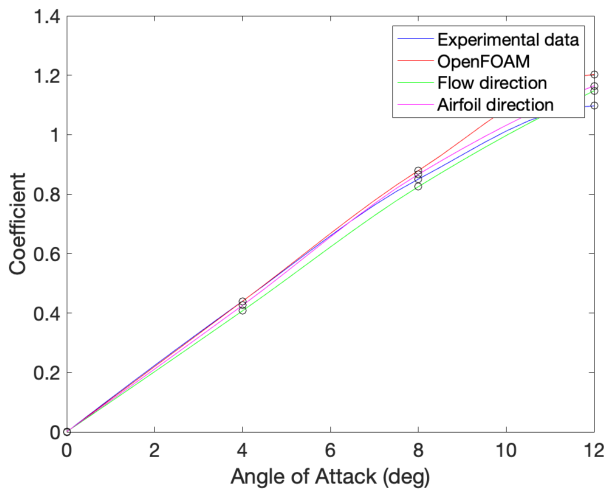

Figure 3.6: Investigation of the mesh alignment evaluating the lift coefficient

Although the absolute error is small, changing the airfoil direction presents less percentage error than any other form. In the drag comparison, the total error that changing the flow direction provokes is 54.14%, while 34.12% if the airfoil is changed. In case of the lift, the flow's error is 3.75% and 2.82% for the airfoil. Breaking down each AoA error, the comparison are shown in Figures 3.7 and 3.8.

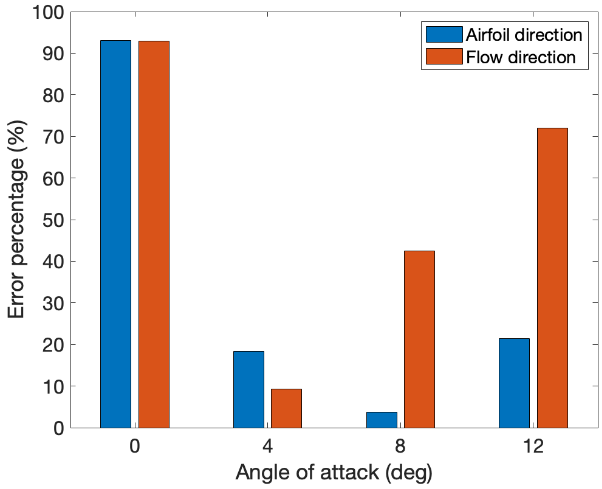

Figure 3.7: Mesh alignment error comparison in the drag coefficient

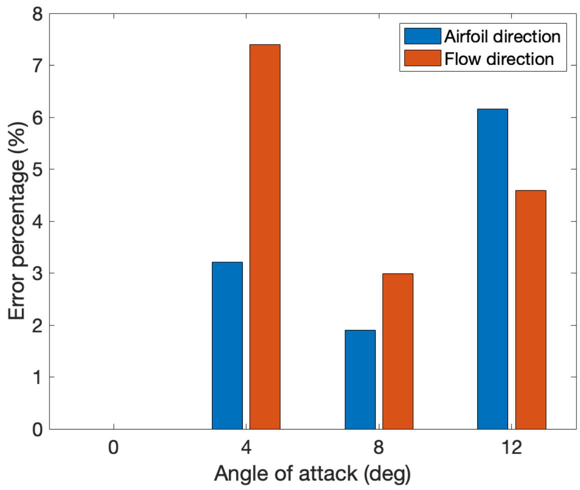

Figure 3.8: Mesh alignment error comparison in the lift coefficient

With the errors, it can be stated that changing the direction of the airfoil shows more accurate and closer results to the experimental data than rotating the incidence angle of the flow. Also, it can be seen in the figures, specially in Figure 3.7, that the error gets bigger with higher angles when changing the flow direction, compared to the airfoil rotation. This can be related to what Warey at al. [35] stated that numerical diffusion reaches it maxima when the streamline direction increases up to 45 degrees.

3.2.3 Transition models

Star-CCM+ offers a wide range of options to define the physics model of the simulation. Specifically, one of the most relevant model that is needed to be set is the transition. As explained previously, this is the phenomenon of laminar to turbulence transition in boundary layers.

The simulation uses unsteady RANS (uRANS) models for $k - \omega SST$ in the 2D situation to capture the flow in the near-wall region, which is less computational expensive than similar models, such as LES or hybrid models [36]. The transition models compared in this investigation are the Gamma Transition and Gamma Re-Theta Transition models. The angles analysed in this section are from 14 to 24 degrees AoA, due to the fact that the stall condition occurs around the 17 degree AoA in a NACA0015 profile [32].

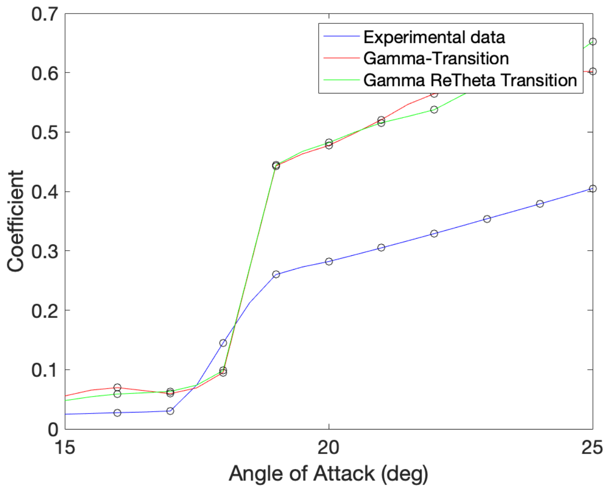

Figure 3.9: Transition model drag coefficient comparison in the transition region from 14 to 24 degree AoA

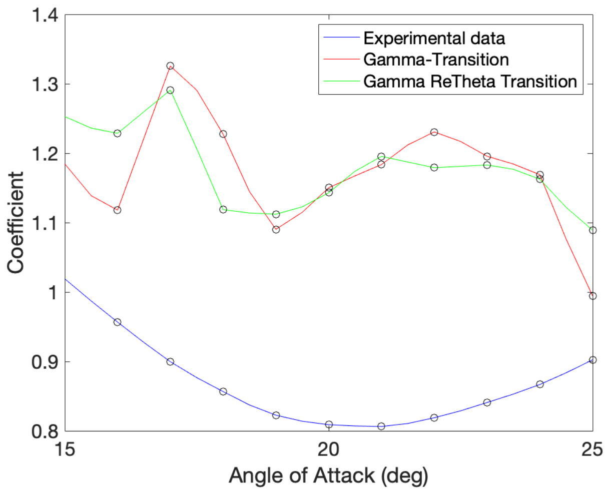

Figure 3.10: Transition model lift coefficient comparison in the transition region from 14 to 24 degree AoA

Both transition models present very similar results but Gamma ReTheta Transition model provides slightly better calculations than the Gamma Transition. More in detail, the Gamma ReTheta Transition model presents an overall error of 71.29% in the drag and 36.68% in the lift. In contrast, the Gamma Transition model shows an overall error of 73.52% in the drag and 36.66% in the lift. Since the errors are really close between both models, they are broken down into each angle of attack to have a more clear perspective of the behaviour, as seen in Figures 3.11 and 3.12.

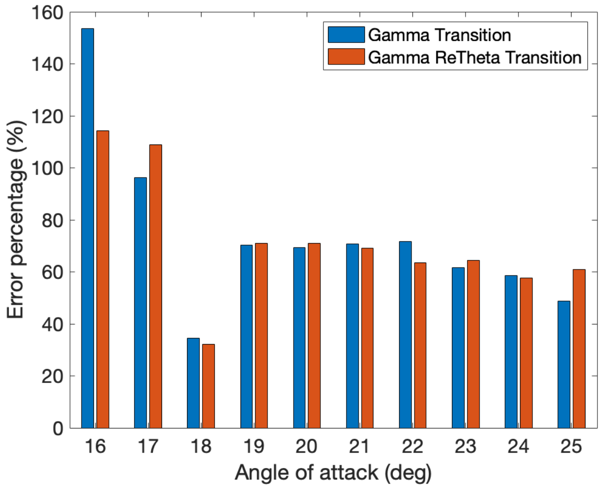

Figure 3.11: Transition model error comparison in the drag coefficient

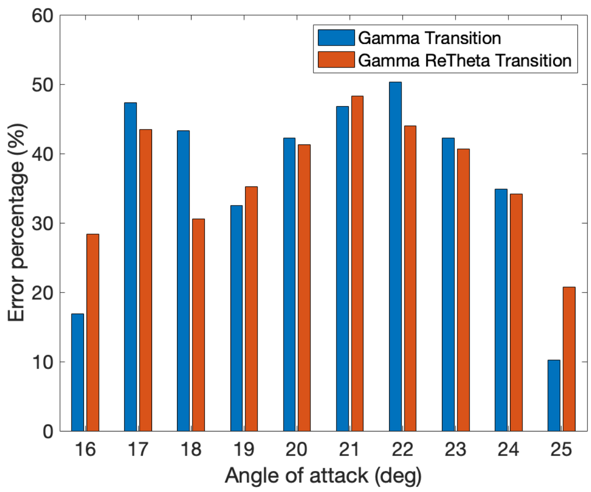

Figure 3.12: Transition model error comparison in the lift coefficient

The Gamma Transition model uses the momentum thickness as a criterion, which happens across the surface. Specifically, it uses the momentum thickness Reynolds number, which is properly described in the commercial software Star-CCM+. For the Gamma ReTheta transition model, a field function can be created to describe the momentum thickness to control the distance from the surface and the intermittency [21]. However, due to the simplicity of the geometry, the functions defined by default by the software are accurate enough to obtain the desirable results so they have not been considered in the setup of the simulations.

The updated model Gamma ReTheta Transition model is advantageous for flow transition on complex geometries [24]. However, the geometry analysed is rather simple. The free-stream conditions are easily identifiable. Therefore, the intermittency values are easily evaluated. Due to this, Gamma Transition model is used in the simulations. Although Gamma ReTheta Transition model presents smaller errors, this model also takes slightly more computational time to solve the simulations than the Gamma model. Perhaps this might happen because the solver has to resolve two additional transport equations, as explained in section 2.3.4.

Both Gamma and Gamma ReTheta Transition models are sensitive to inflow turbulence and can wrongly identify the real location of the start of the transition, in the turbulent layer. In order to avoid a wrong identification, the transition models normally require that the turbulence intensity in front of the object has to be bigger than a certain threshold value [24]. There are two methods to maintain a proper intensity value in front the object [37].

- Calibrate and adjust the turbulence quantities specified at INLET, until the turbulence intensity has got a value bigger than the threshold, by probing in the flow field slightly upstream of the wing.
- Add a source term in the k-eq to counterbalance the loss of turbulence kinetic energy, so that the intensity has been properly maintained upstream the wing.

Neither of these two methods have been tested in this investigation, instead only the default turbulence quantities provided by the solver have been used. This will probably have some consequence on the separation location and frictional force but, this could not be the major error source since there is a large deviation of pressure force (i.e. lift) from the experimental data, meaning that the biggest error source lies somewhere else, as it is explained later.

3.2.4 Courant number

The simulations use an implicit unsteady solver. This approach is based on the time scales of the phenomena of interest. Defining a Courant Number can take a long computational time and space to carry out the investigations. For this reason, the analysis of this parameter aims to compare the modification of the Courant number, the computational time and the accuracy of the results.

	C_L	C_D	Computational time (Vera)
$Experimental$	0.44	0.0105	-
$C = Not - defined$	0.4081	0.0079	<30min
$C_{max} = 1(mean = 0.5)$	0.4107	0.0078	>6h
$C_{max} = 100(mean = 50)$	0.4081	0.0079	<30min

Table 3.1: Courant number analysis 4 degree AoA

	C_L	C_D	Computational time (Vera)
$Experimental$	0.9285	0.0233	-
$C = Not - defined$	1.1743	0.0256	<30min
$C_{max} = 1(mean = 0.5)$	1.1639	0.0244	>6h
$C_{max} = 100(mean = 50)$	1.1741	0.0255	<30min

Table 3.2: Courant number analysis 12 degree AoA

The Courant number definition can truly improve the results as seen in tables 3.1 and 3.2. However, the computational effort is much greater because the Time-Step needs to be increased to meet the number definition. Despite this, the difference of results are really small when comparing them to the experimental data, what leads to conclude that it is more efficient not to define the Courant Number and accept the little error that this creates. The Time-Step used in the simulation is set to be 0.001 seconds having 20 iterations in each TS.

3.2.5 Rotational mesh

With all the previous parameters investigated, a new mesh is created with the objective of improve the working efficiency, as well as improving the results of the investigation. The main characteristic of this mesh is the possibility of rotating the mesh around the airfoil together with the foil. By doing this, there is no need to rotate manually in each angle of attack anymore, now the simulation is set to rotate certain degrees during certain time to evaluate the different conditions automatically. The resulting mesh is shown next.

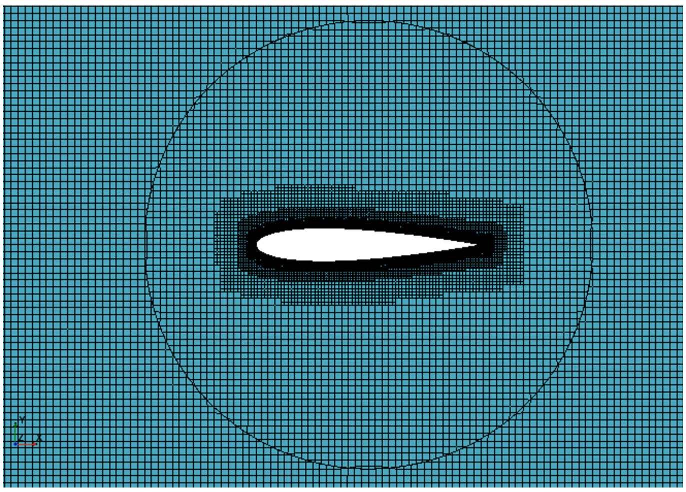

Figure 3.13: Rotational mesh in 2D

Further, the rotational mesh is also used to study the effect of the dynamic stall situation. Modifying the rotational speed, different reduced frequencies can be reached, thus different the dynamic stall responses, as seen in the section 2.1.5.

In order to evaluate the accuracy of this mesh, it is compared next with the experimental data, and the aerodynamic coefficients calculated with the fixed mesh.

The rotation velocity of the mesh is 3 rad/s, what means a reduced frequency of 0.1 (unsteady situation).

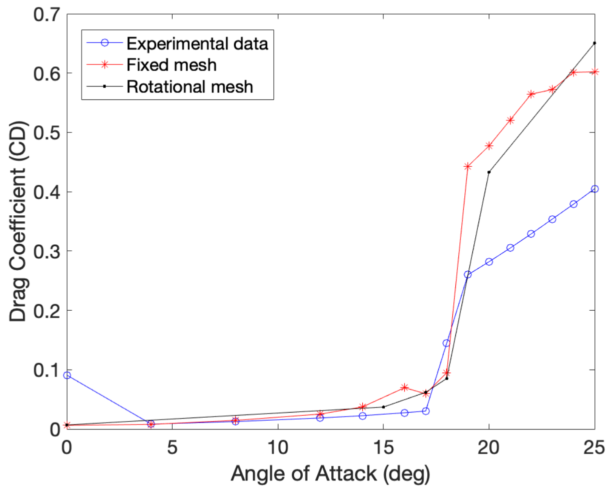

Figure 3.14: Comparison of the fixed and rotational mesh drag coefficients from 0 to 25 degrees AoA

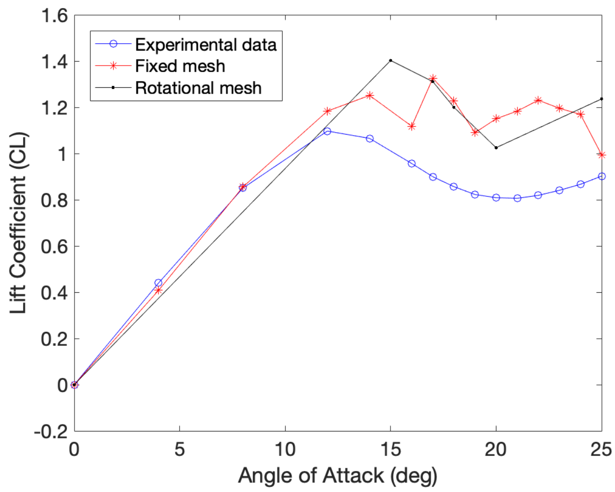

Figure 3.15: Comparison of the fixed and rotational mesh lift coefficients from 0 to 25 degrees AoA

The rotational mesh presents more accurate results with an overall error of 43.79% in the drag parameter and 35.91% in case of the lift compared to the experimental data. The fixed mesh presents an error of 67.83% in the drag coefficient and 37.17% in the lift.

3.2.6 Dynamic Stall

Since the rotational mesh moves with an angular speed, this rotation can create a dynamic stall situation presented earlier in section 2.1.5. The definition of this velocity determines, among others, the delay of the stall condition so it is essential to set it so it does not disturb the results.

As presented in section 2.1.5, one way of controlling the dynamic stall phenomenon is by using the reduced frequency. It is also presented that it exists four main situations for this, a steady state in which the k (reduced frequency) is zero, quasi-steady state with $0 \leq k \leq 0.05$ and unsteady situation with $k > 0.05$ being $k > 0.2$ highly unsteady. For this investigation, the situations that are compared are a quasi-steady state with $k = 0.05$, unsteady state with $k = 0.1$ and highly unsteady state with $k = 0.2$. Since the purpose of this section is to study the effect of the dynamic stall condition and to choose the optimal reduced frequency to use it in further investigations, the variation of angle of attack just needs to be between the laminar and the stall region, thus the interval from 0 to 15 degrees of attack is used to investigate the phenomenon as shown in Figures 3.16 and 3.17.

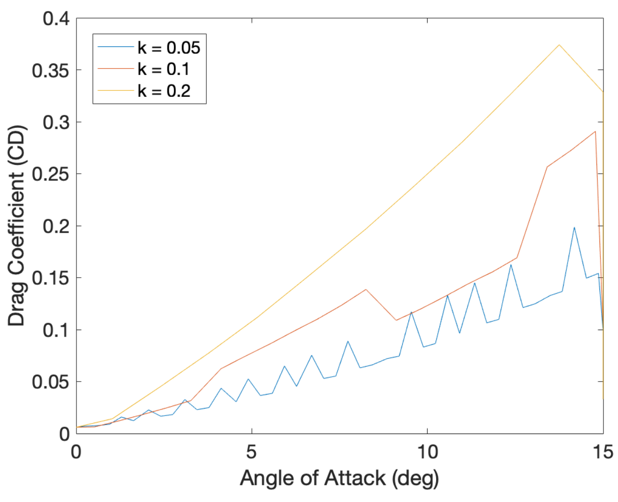

Figure 3.16: Drag coefficients in a dynamic stall situation from 0 to 15 deg depending on the angle of attack

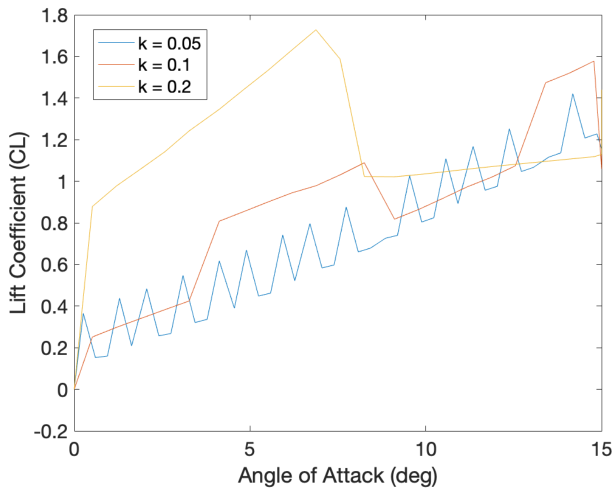

Figure 3.17: Lift coefficients in a dynamic stall situation from 0 to 15 deg depending on the angle of attack

As expected, the higher the reduced frequency is, the faster the wing rotates and the higher the maximum coefficients are achieved. The highest drag and lift coefficient values appear in the highly unsteady reduced frequency situation, when the rotational speed is 6 rad/s. Then, the thrust is higher when this rotation is fast, since the coefficients are larger, as seen in Figures 3.16 and 3.17. Although higher coefficients can be beneficial in the production of thrust, this rapid increase can also have adverse effects in the integrity of the wing when rotating it [38]. Despite this, a speed of 6 rad/s in a one meter chord length is really unlikely to happen.

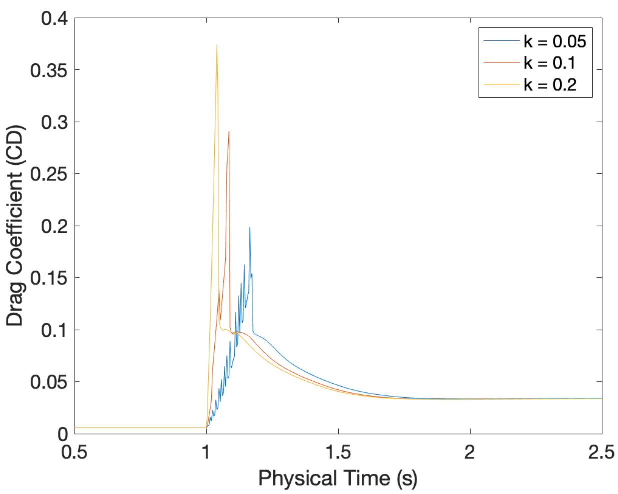

Figure 3.18: Dynamic stall effect in the drag coefficient from 0 to 15 degrees of attack depending on the time

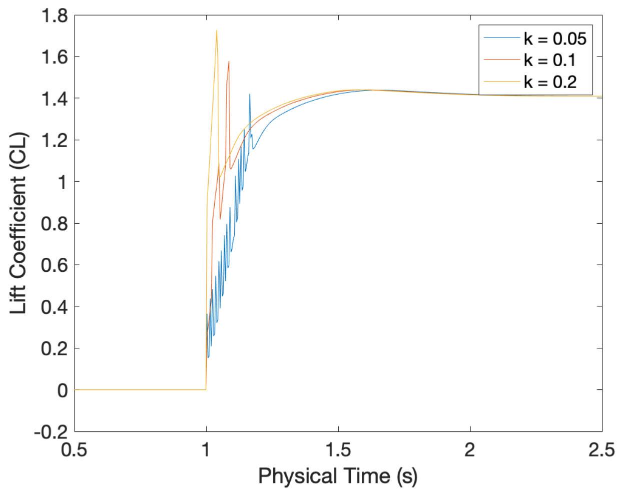

Figure 3.19: Dynamic stall effect in the lift coefficient from 0 to 15 degrees of attack depending on the time

Another interesting aspect to observe is the time that it takes to the flow to stabilize after the rotation is reached, which is observed from the maximum peak of the curve until it gets stable again in the new angle. The longer it takes to stabilize, the more time the higher coefficients are present, thus higher thrust is achieved during a longer period. From another perspective, smaller reduced frequencies take less time to stabilize because it takes longer to completely rotate the foil.

In the overall performance, low reduced frequencies delays the stall situation more than cases where the rotational speed is highly unsteady- high reduced frequencies. However, this delay also implies providing less lift, and thus less thrust, since the increase in the coefficients appear later.

To sum up, the ideal reduced frequency needs to provide a good combination of drag delay and increase in coefficients, which really depends on the application that is wanted. For instance, although a case of a rotational speed of 6 rad/s would provide high thrust, it would definitely also damage the integrity of the structure of a wing such as the Oceanbird's. Then, a case in which the force peaks are not extremely high and the rotational speed is fast enough to delay the stall situation would the best situation. A reduced frequency of 0.1, which results in a rotational speed of 3 rad/s, is the most optimal case of the three studied for this application.

3.3 3D simulations

Two different setups are used when simulating in 3D, a one wing setup and a two wing setup. The one wing setup consists of a single wing inside a "wind tunnel" shaped domain similar to the 2D simulations. It serves to validate the 2D results and at the same time note any differences due to 3D effects. The 3D setup consists of two wings separated by a 1.87m gap between the trailing edge of the front wing and the leading edge of the rear wing. This is a scaled dimension based on the design of the Oceanbird. The two wing simulations will examine the interaction between the two wings and determine the vibration forces on the wings.

3.3.1 Domain

To accurately compute the fluid flow in any CFD application the domain must be the correct size. The domain must be large enough to minimize the effects of blockage and the interaction with the boundaries [39]. However, it must also be small enough so that the computational time does not get too large. A rule of thumb has been proposed that says the domain should extend 2 chord-lengths in front of the airfoil and 5 chord-lengths behind the airfoil [40]. This rule is not exact and needs to be adjusted based on the complexity of the flow. The 3D domain in this investigation is 40 meters long, 16 meters wide, and 15 meters tall. For an airfoil with a 1 meter chord length this goes way beyond the rule presented earlier. Since the flow of a stalled wing has many eddies in the wake a large domain was determined to be necessary.

3.3.2 Mesh Setup

The 3D mesh uses a similar theory to the 2D mesh. A trimmed cell mesh with prism layers is used for all 3D simulations. However, there is a difference between the one wing and two wing simulations. In the one wing simulation, a "C" shaped inlet is used as shown in Figure 3.20.

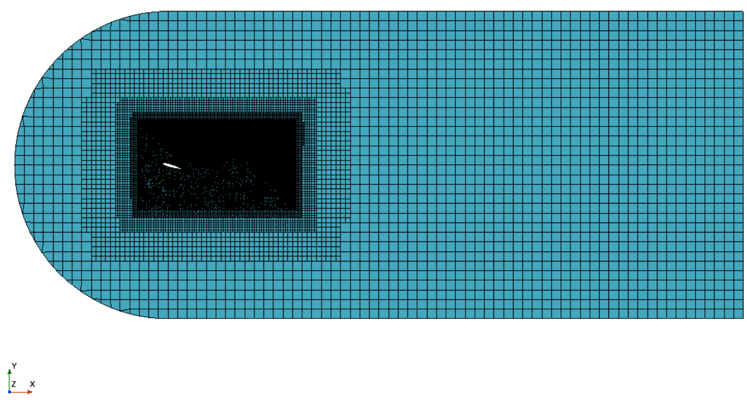

Figure 3.20: "C" Shaped Domain Simulation

This allows the flow to easily be rotated at the inlet. This method was studied and was determined to be inferior to physically rotating the airfoil within the mesh. The two wing simulations use a rectangular domain with a straight wall as the inlet, shown in Figure 3.21. This setup was easier for meshing purposes. It reduces the number of trimmed cells making the mesh simpler to generate and better from a flow perspective.

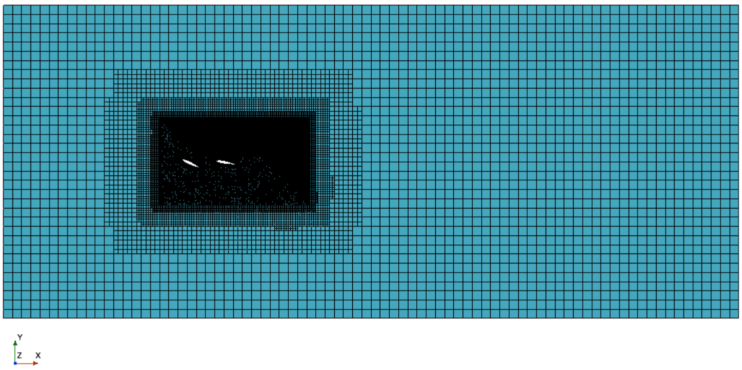

Figure 3.21: Square Domain 2Wing Simulation

If the "C" shaped inlet was kept in the two wing simulation it would have needed a prism layer at the external boundaries. This area is sensitive to flow conditions and disturbances created by the mesh. If the prism layer method is used it will only move the trimmed cells away from the external boundary, not completely remove them. By using the rectangular domain no prism layer is needed at the external boundaries and it does not create trimmed cells at the external boundaries either.

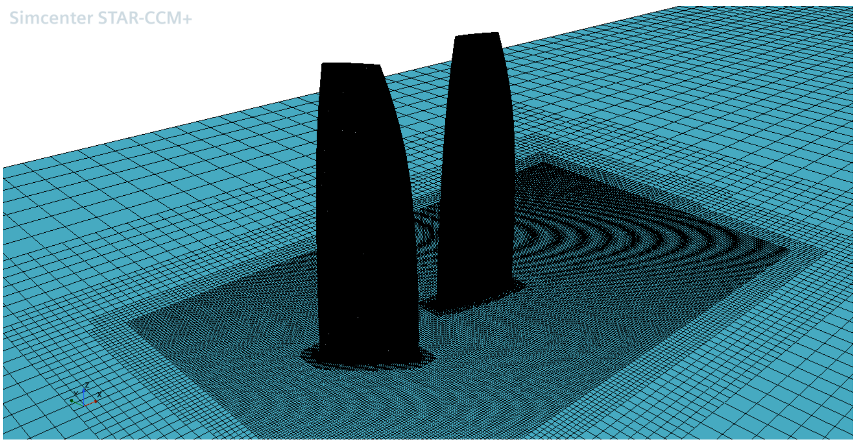

Figure 3.22: Mesh view in 3D of 2 wing simulation

The 3D mesh consists of around 40 million cells distributed over several regions of refinement. Such is so that Figure 3.22's wing profiles present a darker color due to the refinement in this region. In addition to the base mesh there is a refinement around both wings, a prism layer refinement on both wings, a leading edge refinement on both wings, and a surface refinement on the outer surface of both wings. The dimensions are listed in Table 3.3.

	Target Size	Minimum Size
Base Mesh	0.5 m	0.0025 m
Inner Refinement	0.05 m	0.05 m
Leading Edge Refinement	0.0025 m	0.0025 m
Surface Refinement	0.005 m	0.001 m

Table 3.3: Mesh dimensions and refinements for the 3D mesh

The mesh created in 3D has the inner refinement region to accurately and clearly display the wake behind the airfoils. The inner refinement region has dimensions of 8m in length, 4.4m in width, and 4m in height. Besides providing a denser region to more accurately calculate the flow characteristics, this region also helps the transition from the prism layer to the base region. The major dimensions of the prism layer are listed in Table 3.4.

	Value
Number of Prism Layers	20
Prism Layer Near Wall Thickness	$2.3 * 10^{-5}$ m
Prism Layer Total Thickness	$7.5 * 10^{-3}$ m

Table 3.4: Prism layer settings in 3D

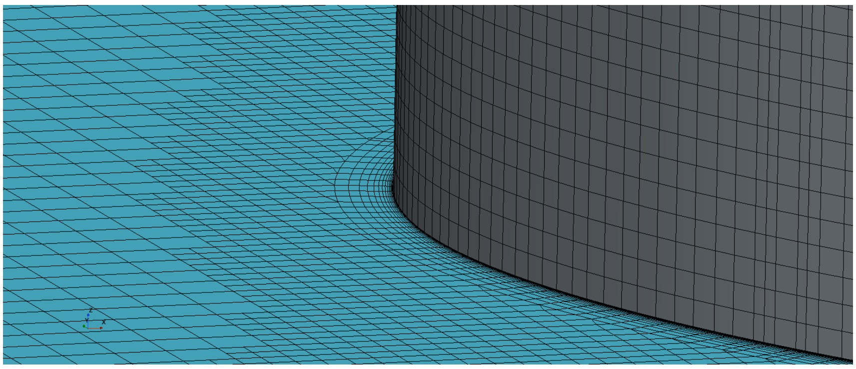

Figure 3.23: Prism layer of 3D mesh

The starting point of the prism layer is the near wall thickness. This is to respect the wall y+ value presented in Section 2.2.3. In order for a near wall model approach to be used the wall y+ value on the first cell of the mesh needs to be around 1. This is satisfied at nearly all points in the mesh except for the tip of the wing and the trailing edge, where there is a small region where it goes above 1. However, at no point does the wall y+ exceed 5 for these simulations, as seen in Figure 3.24.

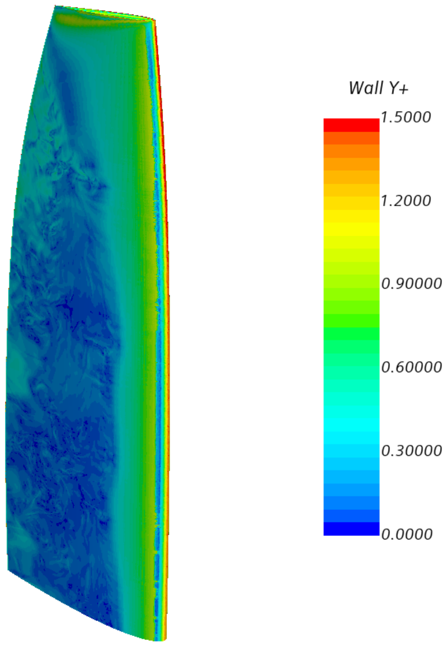

Figure 3.24: $y+$ values along the wing

As seen in equation 2.8, the value of y+ depends on the flow velocity within the near wall boundary region. When calculating the near wall thickness the free-stream velocity value of 15 m/s is used. This overestimates the near wall velocity over a majority of the airfoil but at key points along the airfoil this velocity is higher. In other terms, causing the y+ to be greater than 1.

3.3.3 Physics Models

In all the 3D simulations the IDDES model is used. The hybrid RANS and LES approach is a trade off between resolving the large eddies and computational effort. The IDDES will utilize a LES approach in detached regions while using a RANS approach within the boundary layer. In Star CCM+ it utilizes the $K - \omega$ model in the RANS regions. In Star CCM+ either the IDDES model is the more advanced formulation of the DES model. It is developed to reduce grid induced separation within the solution. The extra computational cost was seen as necessary to obtain accurate results.

As with the 2D simulations the 3D simulations also use a gamma transition model. Any other model was not considered since the study performed in 2D shows that the difference in results are minimal between the two transition models. It is also chosen to limit any differences between models of the 2D and 3D simulations. Similarly, a Courant Number control was not defined in this simulation. To get it below 1 in all mesh cells would have increased the computational time beyond what is reasonable.

3.3.4 Test Cases

As 3D simulations take much more computational power to analyze, the 3D simulations had to be chosen more carefully. For the single wing simulations the focus becomes on the zone from stall to immediately post stall. The AoAs investigated of the single wing ranges from 17 degrees to 45 degrees in this test.

When looking at the two wing case a total of 12 simulations are run, with 7 different AoAs on the front wing and 2 on the rear. The test cases are shown in table 3.5

Front Wing AoA (degrees)	Rear Wing AoA (degrees)
10	10
15	15
25	10
	15
45	10
	15
60	10
	15
90	10
	15
120	10
	15

Table 3.5: Two wing research matrix

These test parameters give a good range of data that includes un-stalled and stalled cases. Computing with two un-stalled AoAs at the rear can show if one AoA or the other is better when following a deeply stalled front wing. The AoAs were chosen to have the leading wing have a near stall condition, several deeper stalled conditions, and finally a condition where the trailing edge is upstream of the leading edge. Having a wide range of configurations allows general conclusions to be drawn, though more specifics will need to be done in future work.

4

Results

Firstly, the results from the 2D-simulations are shown. This includes the comparison of the lift and drag coefficients to the wind tunnel data in every angle of attack from 0 to 180 degrees. Secondly, the 3D results are shown. The one-wing simulations are presented and compared to both the wind tunnel experiments as well as to the 2D-simulations presented in this report. Finally, the two-wing simulations are presented. The response of the first wings AoA is compared on two different non-stalled rear wings. The vibration response and loading is also presented for all 3D-simulations.

4.1 2D-simulations

This section exposes the results obtained in the 2D simulations. The aerodynamic coefficients of the drag and lift are then resolved from 0 to 180 degrees of attack.

4.1.1 Lift and drag coefficients

The 2D simulations aim to study the response of the mesh under every angle of attack. For this reason, the selected mesh resolves the aerodynamic coefficient for the angle of attack from 0 to 180 degrees.

As presented earlier, the final selected mesh is the rotational grid. This mesh resolves the problem from 0 to 180 degrees of attack by changing the angle every certain time that is defined through a field function. This physical time is predefined as it is shown in Figure 4.1 in every angle of attack. With the dynamic stall investigation carried out in section 3.2.6, the rotational speed that is used to change the AoA is 3 rad/s.

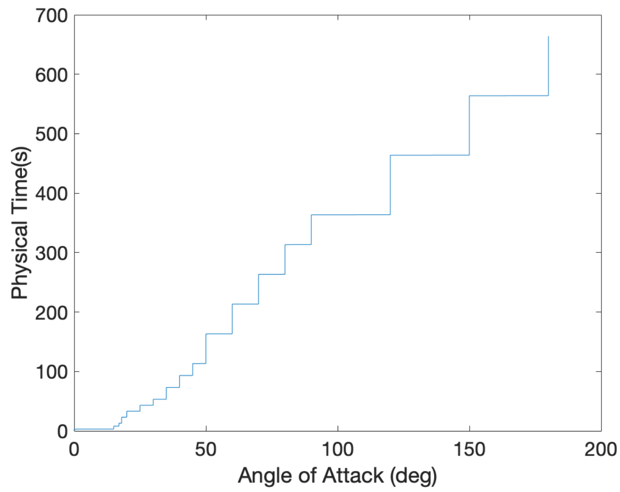

Figure 4.1: Definition of the physical time in every angle of attack calculated

Although the unsteady Reynolds Averaged Navier Stokes (uRANS) model calculates the representative behaviour of non-dynamic, time-averaged eddy behaviour, leading to less chaotic wiggles [24], it is observed that as the angle of attack gets higher, more instabilities appear and more physical time is needed. For this reason, small angles of attack are set to have a low simulation time while the highest angles reach 100 seconds of physical time.

The total physical time is 700s. With a time-step of 0.001s and 20 iterations, the total number of iterations is 14 million. Setting 480 Central Processing Unit (CPU)s in the Vera cluster, the computational speed is 36.65 iterations per second. This leads to a total computational time of 4 days and 11h.

Figures 4.3 and 4.2 show the comparison between the selected mesh and the experimental data. The yellow range defines the maximum and minimum peak of the solution's wiggle at each AoA studied.

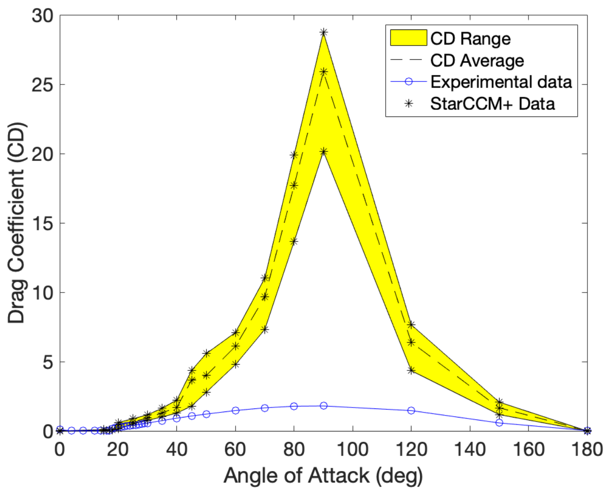

Figure 4.2: Drag coefficient of the 2D simulations for angles of attack between 0 and 180 deg

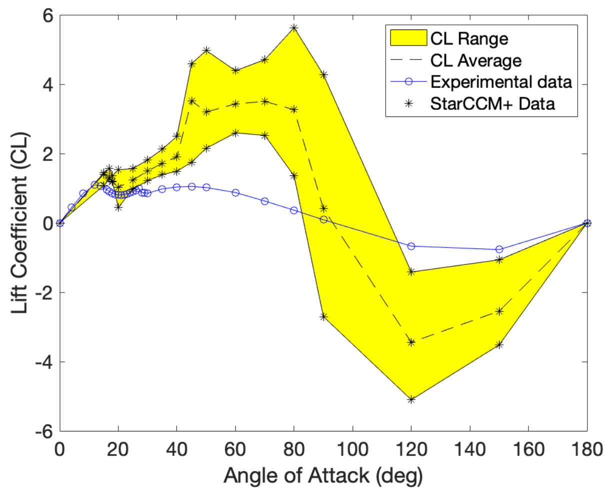

Figure 4.3: Lift coefficient of the 2D simulations for angles of attack between 0 and 180 deg

As expected (defined in section 2.1.1), the drag coefficient hits its maximum value when the AoA is 90 deg, while the lift component reaches its absolute maximum in the 45 deg and 120 deg of attack. Also, the wiggles appear to be bigger around the 90 degree of attack as it can be noticed due to the larger error region. One possible reason for this is that the shape of the time-averaged velocity is forged by the small, mid-sized, and large eddies, which are greater when the airfoil is perpendicular to the flow [24].
Both lift and drag coefficient graphs show a clear error, which represents an error of 257.9% in the drag and 118.5% in the lift component compared to the experimental data [32]. Simulations run in high angles of attack can be challenging due to solution hysteresis. This can be noticed in the low angle of attack region, where the error is around 40% both in the lift and drag coefficients as seen in Figures 4.4 and 4.5.

In this region, which represents the interval between 0 and 30 degrees of attack, the flow has not achieved a turbulent behaviour yet but a transition from attached to turbulent instead.

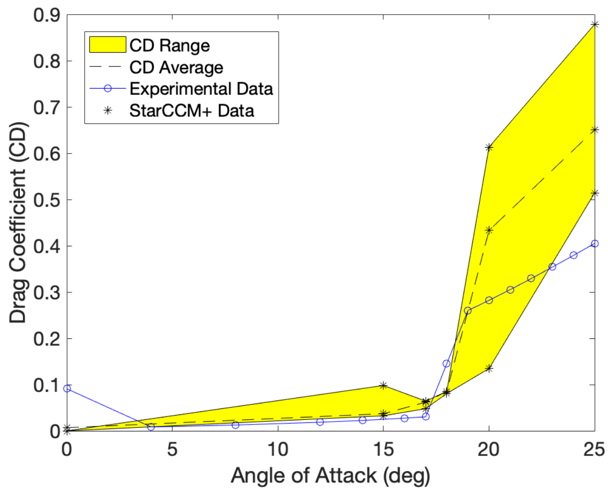

Figure 4.4: Drag coefficient of the 2D simulations for angles of attack between 0 and 30 deg

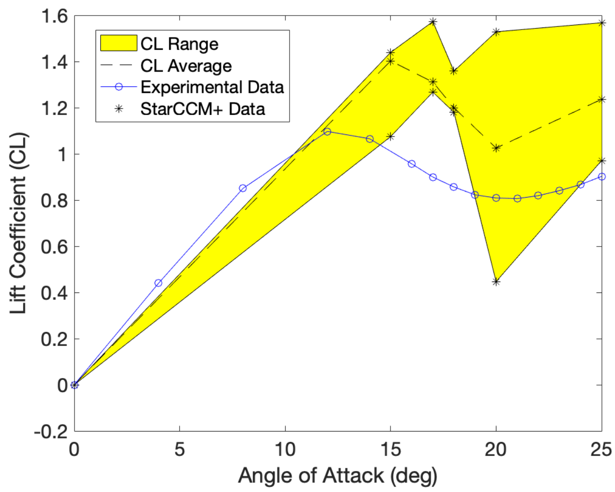

Figure 4.5: Lift coefficient of the 2D simulations for angles of attack between 0 and 30 deg

Deeper into this, when high angles of attack simulations are run as a single instance, they show a separated flow on the top surface indicating stall. This phenomenon occurs in angles where the stall situation is not supposed to appear yet, according to the experimental data. In fact, this situation happens when the stall mechanism is trailing edge stall, which occurs slowly, peeling the boundary layer from the trailing edge along the surface. Increasing the angle of attack, the amount of separation also increases, which continues until stall appears [41].

According to Siemens support [41], one way of avoiding this behaviour can be by starting the simulation at a low angle of attack and rotating the foil through small intervals, what can allow the trailing edge separation develop naturally leaving the flow on the top of the surface still attached. Moreover, when the simulation starts from a high AoA, the slow separation needed to allow natural separation is not develop because of the sensitivity of the separation point. For this reason, the rotational speed defined should have been smaller so the separation of the flow would happen slower too. In this case, each angle has been rotated from the previous one, what means that, in high AoA, the flow, which is already detached and destabilized, gets even more uncontrolled. Then, the larger the angle, the larger the error.

With this, in order to improve the aerodynamic results, either the physical time needs to be increased greatly or the rotation of the airfoil has to start from an attached situation and be increased to the desired angle slowly. However, both alternatives need a lot of computational power, which is limited in this project.

4.2 3D-simulations

The results presented in this section are all based on the IDDES method, using default controls within Star CCM+. Additionally, the mesh used in the following results is presented in the methods.

4.2.1 3D Lift and Drag Coefficients

The lift and drag coefficients calculated in 3D are seen as being a better representation of the flow. This is because 3D end effects are incorporated into the calculation. The wind tunnel test data used throughout this study is meant to mimic a 2D simulation, therefore differences are expected between the 3D CFD results and the 2D experimental data. The differences arise from the end effects. The wind tunnel test has plates attached to both ends, this eliminates any end effects. The 3D simulations were placed in a domain where the bottom edge of the sail rests on the lower boundary of the domain and the top edge of the sail has an 11.5 meter distance from the top of the domain. This means that end effects will influence the flow around the top edge of the sail. It is expected that the 3D CFD results will have lower lift coefficients than the 2D experimental data. Additionally we can expect differences between the 3D results and the full scale Oceanbird ship. The inlet of both the CFD domain and the wind tunnel is fully laminar and no effects were considered from the bottom boundary. On the Oceanbird the deck will have an influence on the flow at the bottom of the sail. Additionally, there will be a gap between the deck and the bottom of the sail which will cause leakage and most likely reduce the lift coefficient of the sail. Finally it should be noted that the trailing edge of the Oceanbird wing tapers so the chord length is longer at the bottom than it is at the top. This makes it even more difficult to compare the 3D model with any previously calculated values of lift and drag.

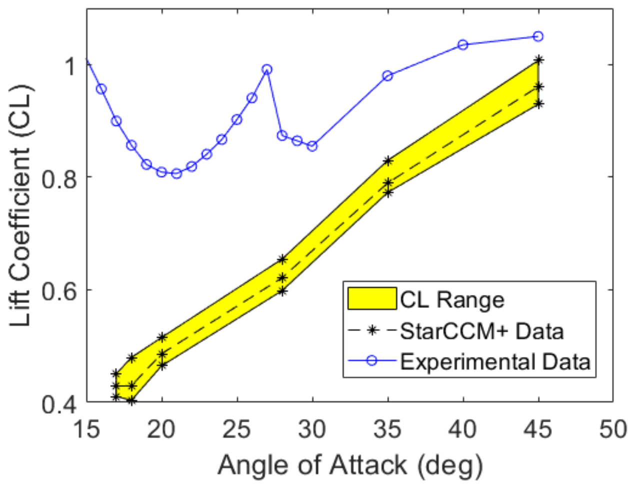

Figure 4.6: Lift coefficient of single wing 3D simulation

In figure 4.6 the measured values of coefficient of lift (CL) are less than the experimental data that it is compared to. That is expected for these comparisons, for the aforementioned reasons. Another aspect not mentioned previously is the aspect ratio. In equation 2.5 a way of correcting these effects is shown. Applying that correction results in between a 4 and 9.6 percent change in the CL. This brings the CFD results closer to the wind tunnel data. Equation 2.5 simplifies a complex set of physics. It confirms that the CL more closely matches the reference data but it has not been applied to the CFD data as a correction factor, since it simplifies the physics too much.

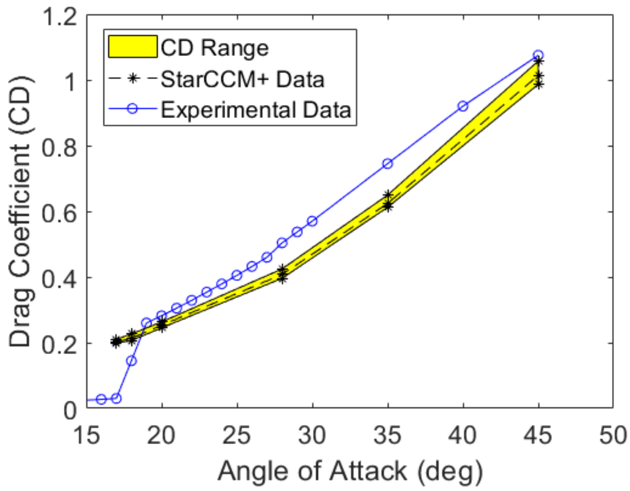

Figure 4.7: Drag coefficient of single wing 3D simulation

The drag coefficient of a single wing seen in figure 4.7 follows a similar trend as the lift. It is generally slightly less than what the experimental results indicate. This could be due to the same reasons as what causes the lift to differ. However, the drag coefficient is more sensitive to mesh issues. This could play a part in the 22 degree result.

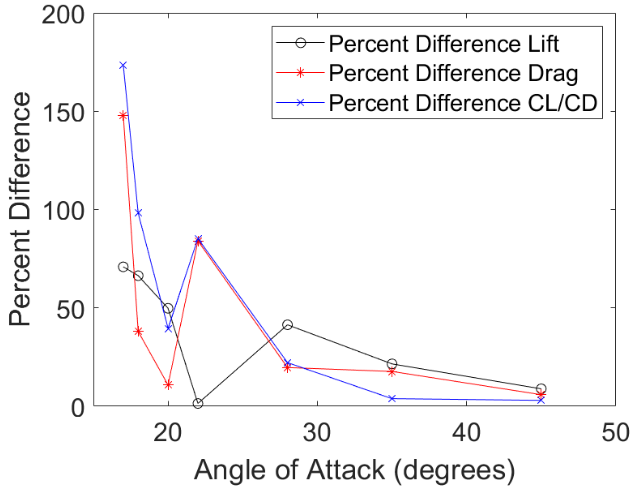

Figure 4.8: Difference between experimental results and 3D simulations

Figure 4.8 summarizes the percentage difference between the wind tunnel data and the 3D CFD results. The large differences at low AoAs is because the CFD simulations indicate that the wing stalls before what the wind tunnel tests show. At higher angles the results are much closer. This is especially evident in the lift drag ratio. At a 35 and 45 degree AoA, the percent difference is only 3.87% and 2.99%. This happens because the lift and drag have proportionally the same error from the wind tunnel data. Individually the error in the lift is 21.54% and 8.87% at the same angles of attack.

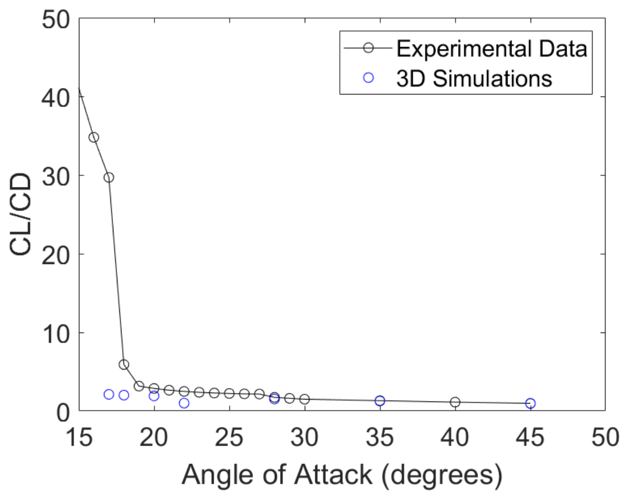

Figure 4.9: Lift drag ratio of single wing 3D simulation

Further evidence of both the earlier stall in the 3D CFD simulations and the closeness of the lift drag ratio at higher angles of attack is shown in figure 4.9. Below the 18 degree AoA the experimental data rises sharply indicating the region of stall. The 3D CFD simulations however, continue without a rapid change showing that the stall occurs at a lower AoA than what is shown. Both lift and drag have decreased when compared to the 2D experimental data. Beyond a 20 degree AoA the lift and drag decreased proportionally so that the lift drag coefficient is comparable to the experimental data.

4.2.2 Comparison 2D simulations with 3D

Once the solutions from the 2D and 3D simulations are obtained, Figures 4.10 and 4.11 show the comparison of both methods.

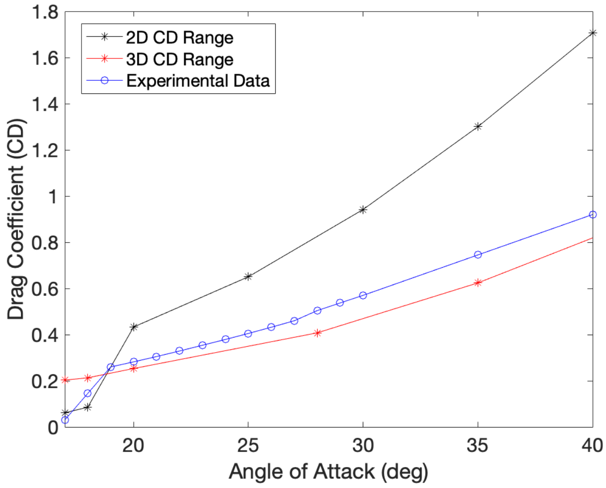

Figure 4.10: Comparison of the drag coefficients of the 2D and 3D simulations

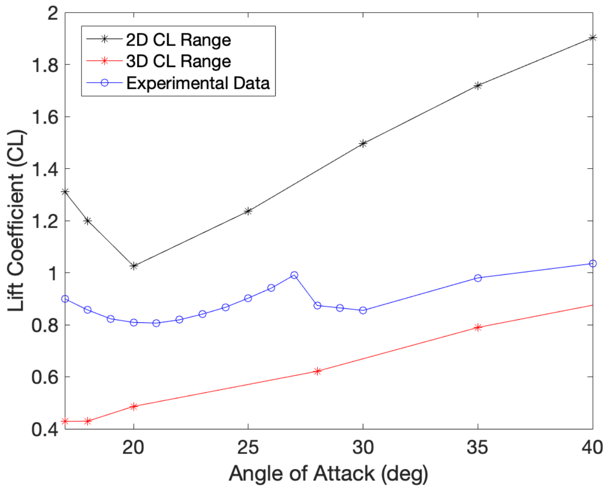

Figure 4.11: Comparison of the lift coefficients of the 2D and 3D simulations

The 3D results generally have better agreement with the reference data than the 2D simulations. Some explanations are that the 3D case include a larger domain, early 2D simulations have a smaller domain, leading to less blockage effects. Other factors include the number of cells, the 3D simulations have approximately double the number of cells which give a finer representation of the flow around the airfoil. Furthermore, the turbulence models are different. In 2D a RANS model is used while in 3D a DES model is used. It is known that the DES model is better at modeling turbulent zones, an area that becomes large at high angles of attack. Lastly, 3D effects are considered in the 3D simulation, where end effects are accounted for.

There are still differences between the Star-CCM+ resolution and the wind tunnel data. The aspect ratios are different in the investigation and the experimental data, the model that is used in Star-CCM+ has a much higher aspect ratio than the one tested in the wind tunnel. But, most of the difference is expected to come from the end effects. The wind tunnel tests had the airfoil mounted to wall inserts inside the wind tunnel, this will most likely cause a slight increase in lift since it reduces the possibility of wingtip vorticies. Despite the differences, the 3D simulations accurately show the lift and drag seen at the angles of attack tested.

4.2.3 3D Multiple Wing Simulations

The results in this section are based on 2 wing simulations. The method for these tests are described in section 3.3.4. The basic setup was to adjust the leading wing through various angles of attack while keeping the trailing wing at a constant angle of attack. These tests were performed for two trailing edge angles of attack, 10 degrees and 15 degrees.

What follows from figure 4.12 to figure 4.16 shows the lift and drag coefficients of the rear wing at both 10 and 15 degrees. In addition to the average CL and coefficient of drag (CD) for every front wing AoA, the maximum and minimum are displayed in the yellow range.

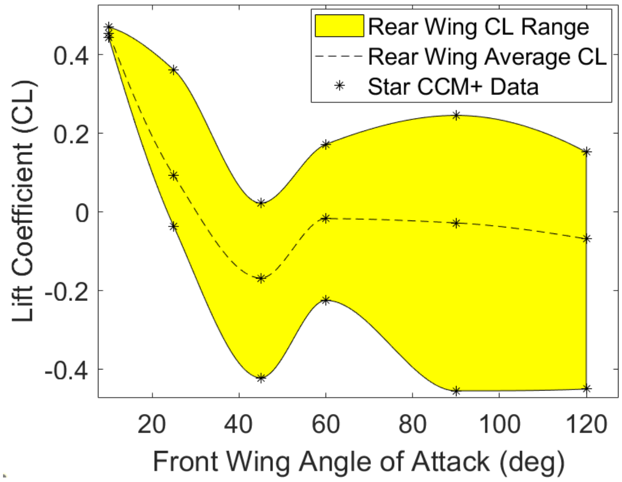

Figure 4.12: Rear wing lift coefficient with 10 degree AoA

The smallest AoA tested for both cases matched the AoA of the rear wing. Shown in the following figures it can be seen that the range of lift and drag coefficients are small at 10 and 15 degrees. This is because the wing has fully attached flow, as shown in the 10 degree case, or it has partially separated flow, as shown in the 15 degree case. With a stalled front wing the range of lift and drag coefficients increases dramatically. The highest range is seen with a 90 degree AoA front wing. The large range in lift values is due to the eddies being shed by the forward wing. These flow structures are shown to have a major effect on the lift and drag of the rear wing. More about these eddies and the forces caused by them are discussed in section 4.2.4

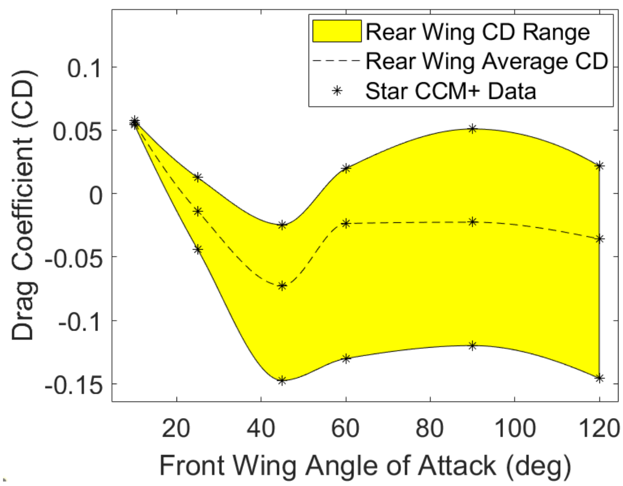

Figure 4.13: Rear wing drag coefficient with 10 degree AoA

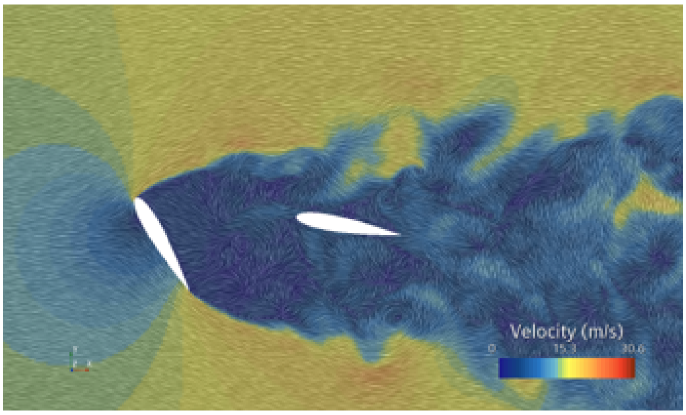

Figure 4.14: Velocity vector scene of two wings; one at 60 degrees the other at a 10 degree AoA

The rear wings experienced reduced lift even in the attached configuration. Once the leading wing becomes stalled the rear wing ceases to produce lift except during the oscillations seen from the eddies being shed from the leading wing. Comparing the average lift coefficient of the rear wings with the experimental results, it is determined that the rear wing is effected severely by the wake of the front wing. This happens in all configurations. At a 15 degree AoA the CL on the 15 degree AoA rear wing is reduced by 31.6% compared with experimental. At a 25 degree AoA the CL on the rear wing is reduced by 75% compared with experimental. Finally, at AoAs above 45 degrees the lift is reduced to zero. The results are similar when the rear wing is set to 10 degrees. When the front wing is at a 10 degree AoA the rear wing looses 55.2% of its CL, at a 25 degree AoA the rear wing looses 90.9% of its CL and anything beyond 45 degrees the rear wing looses 100% of its CL.

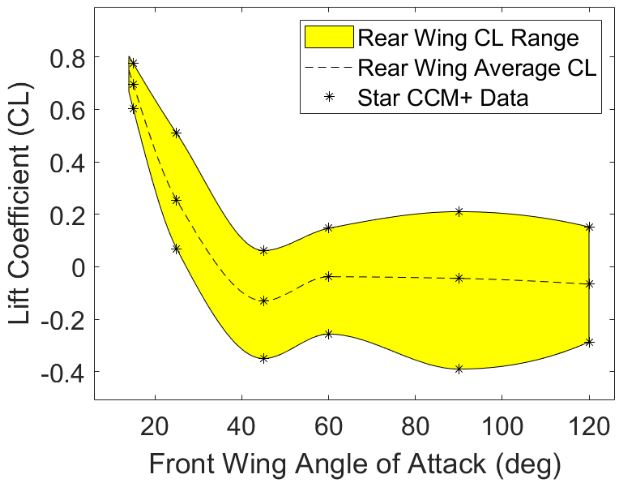

Figure 4.15: Rear wing lift coefficient with 15 degree AoA

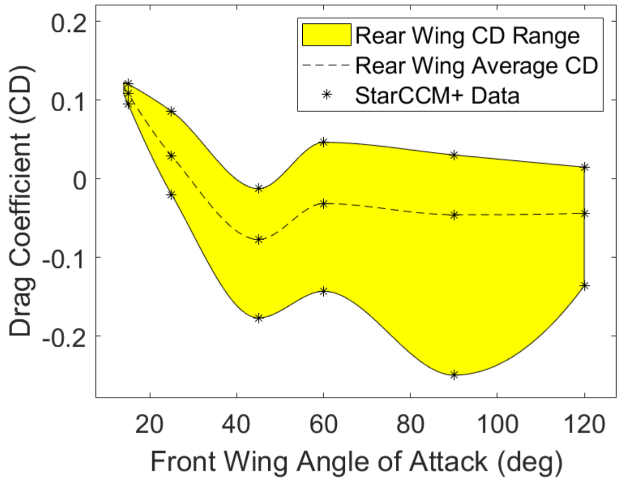

Figure 4.16: Rear wing drag coefficient with 15 degree AoA

For rear wing simulations at both 10 and 15 degree AoA the airfoil experiences both positive and negative lift and drag. Since the airfoil is a symmetric shape it is easily understood that it can produce both positive and negative lift based on the angle of attack and whether it is pitching up or down. It is less intuitive to think about a negative drag. A negative drag in this context means that the rear wing is being pulled forward by the drag component of the flow. It seems like it is impossible, but at the angles of attack in question the airfoil is acting more like a wall. In a paper by Ethirajan Rathakrishnan, he studied the flow around a flat plate and noticed areas of backflow [42]. These are areas where the vorticies being shed by the plate create a reverse flow directly behind the plate. This is the most likely scenario of why this happens during the high AoA simulations.

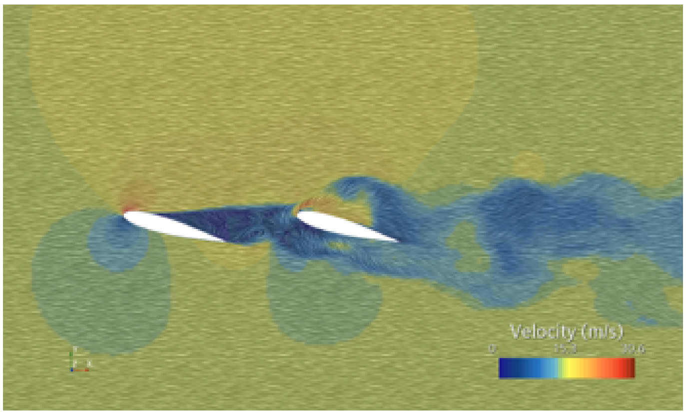

Figure 4.17: Velocity vector scene of two wings at 15 degree angles of attack

4.2.4 Vibrations

The frequencies where vibration loads are likely to occur on the wing are calculated using a single sided FFT spectrum within Matlab. The raw data can be seen in the appendix, only the higher amplitude frequencies are presented in this section.

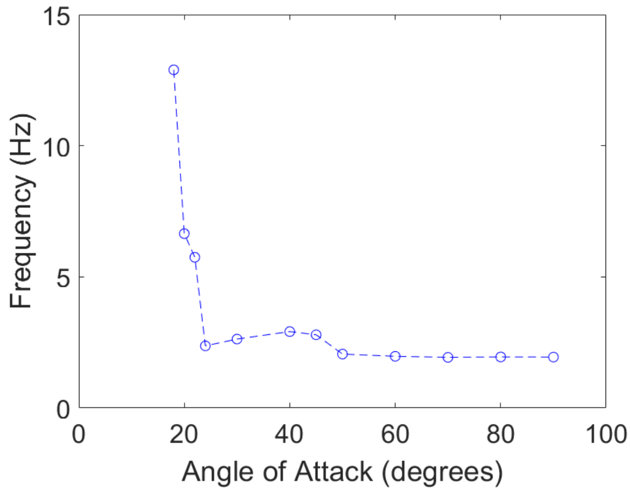

Figure 4.18: Vortex shedding frequency on one wing

The results in figure 4.18 indicates that the primary vortex shedding frequency is consistent at higher angles of attack. Above a 45 degree AoA the frequency is consistent around 2 Hz. At lower AoAs the vortex shedding frequency is much higher but the amplitude is reduced greatly. That means the lower AoA configurations does not have one single frequency dominating and is in general not affected as much from this type of vibration. Then, the results from the frequency calculations show that the the high angles of attack, this is, stall situations, should be avoid. Otherwise, the whole integrity of the wing would be compromised.

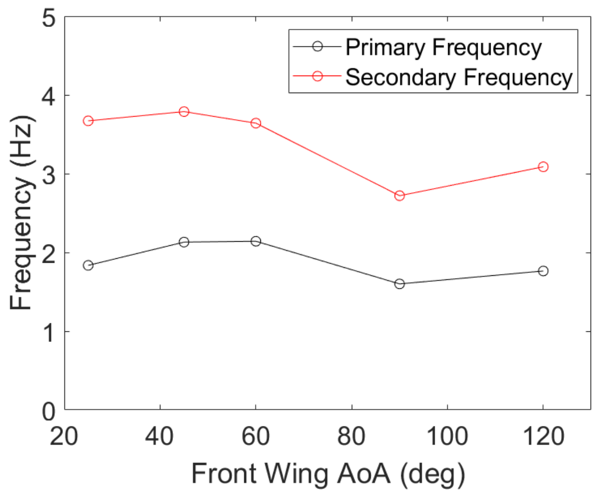

Figure 4.19: Vortex shedding frequency on rear wing with an AoA of 10 degrees

The results in figures 4.19 and 4.20 are different than the results in figure 4.18. Normally a 10 or 15 degree AoA will not produce noteworthy vibrations because the flow is still mainly attached. These vibrations are being caused by the additional wing upwind, with the leading wing AoA noted along the x-axis. That is the major source of the vibrations but it also is caused by the interaction between the two sails as the 10 and 15 degree AoA have different vortex shedding frequencies.

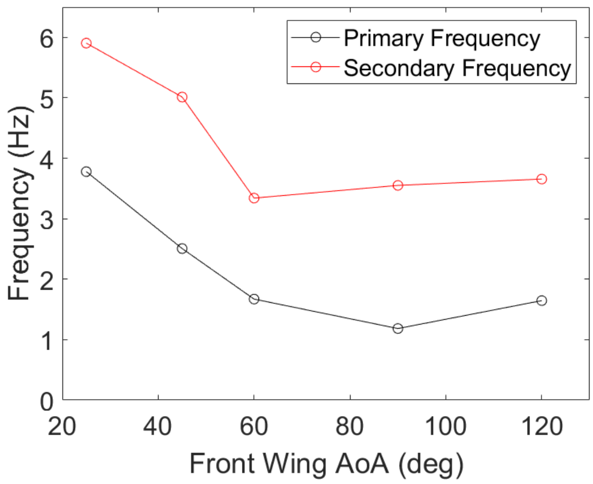

Figure 4.20: Vortex shedding frequency on rear wing with an AoA of 15 degrees

Despite the same front wing AoAs being used in both 3D two wing simulations, the resultant vortex shedding frequencies are different for a 10 degree and 15 degree rear wing. This means that the interaction of the rear wing has an effect despite having the same inflow. In the primary frequency the difference between a 10 degree AoA and a 15 degree AoA is between 6.97% and 29.91% depending on the rear wing AoA. The frequencies with the second highest amplitude follows a similar trend, with a difference of between 8.59% and 27.83%. Meaning that the frequency on the trailing wing can be controlled by its AoA under these conditions.

4.2.5 Forces

With a chord length of 23 meters and a span of 80 meters the forces on an airfoil of this size is immense. To quantify these forces, the resultant force exerted on the airfoil is calculated and applied through the center of effort of the sail, also called the geometric center of the sail. The force exerted has a direct relationship to the lift and drag coefficients. Therefore the worst case scenario is presented, at an angle of attack of 45 degrees. In this configuration the sail exerts a maximum torsion moment of 17.74 MN-m and a maximum bending moment of 61.71 MN-m. Nothing can be said of the strength of the rig, as this design was not provided for this report. But, it should be noted that these forces exist and will need to be accounted for when the design and material selection are finalized.

5
Conclusion

It has been determinant dividing the project into two parts, 2D and 3D simulations. Each part has relied in the other one, improving the simulations, leading to a more precise investigation. The 2D simulation has been used to analyse and investigate different aspects needed to carry out the 3D simulations. This last part investigated the main aim of the project, which was study both the behaviour of the Oceanbird's wing under different situations and the response of multiple wings by using CFD.

5.1 2D-Simulations

The 2D simulations have shown the importance of creating an appropriated mesh for the investigation. In this case, the uRANS model has been used to mainly capture the flow in the boundary layer, which specially affected this simulation. For this reason, a refinement around the foil has also been needed, more precisely in the leading edge, trailing edge and suction area, regions where the instabilities appear first. Further into the mesh analysis, the influence of the mesh direction has been investigated, observing that the alignment of the flow with the cells is of great importance. The numerical diffusion can be minimized if the airfoil is rotated instead of rotating the whole mesh. The Courant number has also been analysed, observing that it did not affect the solution, so it has been decided to leave it undefined.

In relation to the physic models, two transition models have been compared as well, Gamma Transition and Gamma ReTheta Transition model. It has been concluded in this part that both models presented really similar results but, since the second model took longer time to compute and geometry analysed is simple, Gamma Transition model has been used. Finally, as one of initial aims of the 2D simulations was investigating every AoA from 0 to 180 deg, a rotational mesh has been created. This mesh could be rotated automatically by defining a field function. This mesh has resulted to be more accurate than the fixed mesh.

Once the 2D-mesh has been created, the dynamic stall phenomenon has been analysed. Three cases have been used for the investigation, where the rotational speed is changed. The final conclusion of this part has been that both the integrity of the structure and the thrust production need to be considered, a combination of both parameters variate depending on the application. In this scaled case, the resulting rotational speed has been chosen to be 3 rad/s (reduced frequency k = 0.1). However, with a bigger wing, such as the Oceanbird's, this rotational speed needs to be decreased considerably not to compromise the structure.

With all this, the investigation of the drag and lift coefficients has been performed from 0 to 180 degrees of attack. It has been observed that, for low AoA (from 0 to 30 deg), the simulation performed good when comparing it to the experimental data. However, the larger the AoA is, the higher the error becomes. Although it has not been corrected due to the computational time, it has been observed that either the physical time can be increased to stop the unsteadiness, or the rotation of the mesh has to go from an attached region to the desired high AoA.

5.2 3D-Simulations

Several key findings are made when performing CFD simulations in 3D. Firstly, the lift and drag coefficients do not match the experimental data that was used. However, despite this mismatch it looks like an acceptable result when considering all the factors. Secondly, the multi-wing analysis shows that the trailing wing has reduced lift compared to the leading wing. This holds true for any angle of attack with the worst loss of lift occurring when the trailing wing is following a stalled leading wing. Finally, the main vibration on the airfoil becomes fairly consistent at high angles of attack making it easy to design the structure around. When looking at two wings it is shown that the angle of attack of the rear wing can cause a change in the frequency despite having the same inflow from the preceding wing. This makes it easier to control the vibrations on the trailing wings if there is a stalled leading wing.

The lift and drag on a single wing in 3D, at first glance, appear to differ somewhat. But looking closely into several factors makes sense of this difference. The nature of the wind tunnel test is seen as the biggest contributing factor. Both ends of the NACA 0015 section were mounted to the wall of the test section. This simulates a wing without end effects. While this is accurate for comparisons with 2D CFD tests it does cause a difference when looking at 3D results. Other contributing factors include, both differing aspect ratios and chord length differences.

At any angle of attack the trailing wing is shown to have a reduction in lift compared to a leading wing. In attached flow conditions the rear wing experiences a 31.6% reduction in lift. This increases in stalled conditions where the rear wing loses 100% of its lift in many configurations. This is not a concern under normal operating conditions. However, if one of the forward sails malfunctions and becomes stalled, the sail immediately aft will not have any lift available either. The reduction of lift in the attached flow conditions is not a surprise either and is simply a factor that will need to be kept in mind when calculating the total thrust output of the sails. While many of these results are expected, the appearance of negative drag was not. A possible explanation of this is the appearance of backflow behind the leading wing. It has been reported that this can occur on wall shaped geometry but no specific information could be obtained from the results in these simulations.

The vortex shedding frequency is studied as a way to estimate what oscillatory loads will be put onto the wings. Without a detailed view of the sail structure nothing much can be said about whether certain frequencies are harmful or not. It is shown that during the most dangerous angles of attack the frequency is steady around 2 Hz. This fact makes it easier to design a structure that can handle this type of loading. A positive result also comes from the 2 wing simulations. It shows that the angle of attack of the rear wing will change the oscillatory frequency when following a stalled wing. This means that if a front wing is stuck in a stalled condition, the rear wing could be tuned so it does not enter a range of harmonic frequencies and damage the structure.

5.3 Future Work

Wallenius Marine hopes to build the first ship by 2025, so future work related to this topic is ongoing. Wind tunnel tests will be necessary to accurately study the forces on the wings. The Oceanbird will have a telescopic system to lower the sails, this system creates a unique shape at the interface between the sections. Meaning the spanwise shape of the the wing along the leading and trailing edge will need to be studied further to fully understand the flow. Additionally, an in-depth structural analysis would be useful for determining the best solutions for building the rig. This could include a FEM analysis or a full fluid-structure analysis of the wing. This would need to include the internal structure of the wing and the mast. Additional work could be performed in this area as well.

Regarding this project, deeper investigations into the high AoA would explain better why Star-CCM+ presented larger errors in this regions than in smaller angles. The possible reasons for this error found in the project need to be proven with the software. In the case of the 3D investigation, since the mesh used has presented good results compared with the experimental data, more test cases in the multiple wings would be interesting to be studied with this grid. This could be backed up by wind tunnel tests, which will be performed this coming fall 2021. Moreover, studying the interaction of more than two wings would make a clearer idea of how the Oceabird would behave in extreme conditions.

Bibliography

[1] S. Wachsmann, *Seagoing ships & seamanship in the Bronze Age Levant.* Texas A&M University Press, 2009.

[2] L. Clancy, *Aerodynamics.* John Wiley & Sons, 1978.

[3] "NACA 0015." [Online]. Available: http://airfoiltools.com/airfoil/details?airfoil=naca0015-il

[4] T. K. Guha, W. Oates, and R. Kumar, "Characterization of piezoelectric macrofiber composite actuated winglets," *Smart Materials and Structures*, vol. 24, p. 2, 06 2015.

[5] G. Arvel, *The Aerodynamics of Sail Interaction.* The Third AIAA sympsium, 1971.

[6] K. Mulleners and M. Raffel, "Dynamic stall development," 2013. [Online]. Available: https://doi.org/10.1007/s00348-013-1469-7

[7] S. McGrail, *Boats of the world: from the Stone Age to medieval times.* Oxford University Press on Demand, 2004.

[8] R. Anderson and C. Anderson, *The sailing-ship: six thousand years of history.* G.G. Harrap Limited, 1947.

[9] S. Jefferson, *Clipper Ships and the Golden Age of Sail: Races and rivalries on the nineteenth century high seas.* Bloomsbury Publishing, 2014.

[10] M. E. Fletcher, "The suez canal and world shipping, 1869-1914," *The Journal of Economic History*, vol. 18, no. 4, pp. 556–573, 1958.

[11] G. S. Graham, "The ascendancy of the sailing ship 1850-85," *The Economic History Review*, vol. 9, no. 1, pp. 74–88, 1956. [Online]. Available: http://www.jstor.org/stable/2591532

[12] N. Patrick, "The beautiful Pamir: The world's last commercial sailing ship," Oct 2016. [Online]. Available: https://www.thevintagenews.com/2016/06/24/the-beautiful-pamir-the-worlds-last-commercial-sailing-ship/

[13] B. Clayton, "Wind-assisted ship propulsion," *Physics in Technology*, vol. 18, no. 2, p. 53, 1987.

[14] H. K. Versteeg and W. Malalasekera, *An introduction to computational fluid dynamics: the finite volume method.* Pearson education, 2007.

[15] "STAR-CCM+." [Online]. Available: https://www.plm.automation.siemens.com/global/en/products/simcenter/STAR-CCM.html

[16] S. Martínez-Aranda, A. García-González, L. Parras, J. Velázquez-Navarro, and C. Del Pino, "Comparison of the aerodynamic characteristics of the NACA0012 airfoil at low-to-moderate reynolds numbers for any aspect ratio," *International Journal of Aerospace Sciences*, vol. 4, no. 1, pp. 1–8, 2016.

[17] "Downwash effects on lift," 2021. [Online]. Available: https://www.grc.nasa.gov/WWW/K-12/airplane/downwash.html

[18] S. Yon and J. Katz, "Study of the unsteady flow features on a stalled wing," 1997.

[19] "Dynamic stall," 2021. [Online]. Available: https://afcad.osu.edu/dynamic-stall

[20] G. J. Leishman, *Principles of Helicopter Aerodynamics.* Cambridge Aerospace, 2016.

[21] "STAR-CCM+ tutorials," 2021.

[22] J. Frohlich, C. Mellen, W. Rodi, L. Temmerman, and M. Leschziner, "Highly resolved large-eddy simulation of separated flow in a channel with streamwise periodic constrictions," *Journal Fluid Mech*, pp. 19–66, 2005.

[23] M. Van Dyke, *An Album of Fluid Motion*, 1982.

[24] S. Rodriguez, *Applied Computational Fluid Dynamics and Turbulence Modeling.* Sandia National Laboratories, Albuquerque, NM, USA: Springer, 2019. [Online]. Available: https://doi.org/10.1007/978-3-030-28691-0

[25] S. Leonardi and I. Castro, "Channel flow over large cube roughness: a direct numerical simulation study," *Cambridge University Press*, 2010.

[26] "Turbulence part 3 - selection of wall functions and y+ to best capture the turbulent boundary layer," 2013. [Online]. Available: https://www.computationalfluiddynamics.com.au/category/tips-and-tricks/

[27] L. Larsson and H. Raven, *Ship resistance and flow*, J. Paulling, Ed., 2010.

[28] H. Schlichting and K. Gersten, *Boundary-Layer Theory.* Springer Berlin Heidelberg, 2017. [Online]. Available: https://search.ebscohost.com/login.aspx?direct=true&db=cat07472a&AN=clec.SPRINGERLINK9783662529195&site=eds-live&scope=site

[29] M. Heideman, H. Johnson, S. Burrus, and C. Sidney, *Gauss and the history of the fast Fourier transform*, 1984.

[30] H. J. Nussbaumer, "The fast fourier transform," in *Fast Fourier Transform and Convolution Algorithms.* Springer, 1981, pp. 80–111.

[31] C. Maklin, "Fast fourier transform," Dec 2019. [Online]. Available: https://towardsdatascience.com/fast-fourier-transform-937926e591cb

[32] R. Sheldahl and P. Klimas, *Aerodynamic Characteristics of Seven Symmetrical Airfoil Sections Through 180-Degree Angle of Attack for Use in Aerodynamic Analysis of Vertical Axis Wind Turbines*, 1981.

[33] H. Zhu, "CFD investigation of wind-powered ships under extreme condition: Simulations on the naca-0015 foil under deep stall condition," 2020. [Online]. Available: https://hdl.handle.net/20.500.12380/301919

[34] J. Jansen and J. Nilsson, "Application of a humpback whale fin as a rudder," 2017.

[35] A. Warey, T. Han, and S. Kaushik, "Investigation of numerical diffusion in aerodynamic flow simulations with physics informed neural networks," 2021.

[36] L. Davidson, *Fluid mechanics, turbulent flow and turbulence modeling*, 2015.

[37] Z. Belfkira, H. Mounir, and A. Marjani, "A new strategy for analysing the impact of turbulence intensity on a horizontal axis wind turbine performances using a computational fluid dynamics simulation," 2021.

[38] S. Yoshida, "Dynamic stall model for tower shadow effects on downwind turbines and its scale effects," *Energies*, 2020.

[39] A. Rezaeiha, I. Kalkman, and B. Blocken, "CFD simulation of a vertical axis wind turbine operating at a moderate tip speed ratio: Guidelines for minimum domain size and azimuthal increment," *Renewable energy*, vol. 107, pp. 373–385, 2017.

[40] "CFD computational domain," Sep 2020. [Online]. Available: https://www.idealsimulations.com/resources/cfd-computational-domain/

[41] "The importance of angle of attack continuation for high angle of attack simulations," 2018. [Online]. Available: https://community.sw.siemens.com/s/

[42] E. Rathakrishnan, "Visualization of the flow field around a flat plate," *Instrumentation & Measurement Magazine, IEEE*, vol. 15, pp. 8–12, 12 2012.

A

Appendix 1

Table 3. (cont)

0	75.0000	.5000	1.7350
0	80.0000	.3650	1.7800
0	85.0000	.2300	1.8000
0	90.0000	.0900	1.8000
0	95.0000	-.0500	1.7800
0	100.0000	-.1850	1.7500
0	105.0000	-.3200	1.7000
0	110.0000	-.4500	1.6350
0	115.0000	-.5750	1.5550
0	120.0000	-.6700	1.4650
0	125.0000	-.7600	1.3500
0	130.0000	-.8500	1.2250
0	135.0000	-.9300	1.0850
0	140.0000	-.9800	.9250
0	145.0000	-.9000	.7550
0	150.0000	-.7700	.5750
0	155.0000	-.6700	.4200
0	160.0000	-.6350	.3200
0	165.0000	-.6800	.2300
0	170.0000	-.8500	.1400
0	175.0000	-.6600	.0550
1	180.0000	0.0000	.0250
1000000.0 NACA 0015 SECTION DATA, EPPLER MODEL, CL, CD, DEC 78			
0	0.0000	0.0000	.0074
0	1.0000	.1100	.0075
0	2.0000	.2200	.0076
0	3.0000	.3300	.0079
0	4.0000	.4400	.0083
0	5.0000	.5500	.0091
0	6.0000	.6600	.0101
0	7.0000	.7700	.0111
0	8.0000	.8504	.0126
0	9.0000	.9387	.0138
0	10.0000	1.0141	.0152
0	11.0000	1.0686	.0168
0	12.0000	1.0971	.0186
0	13.0000	1.0957	.0205
0	14.0000	1.0656	.0225
0	15.0000	1.0145	.0249
0	16.0000	.9567	.0275
0	17.0000	.8996	.0303
0	18.0000	.8566	.1450
0	19.0000	.8226	.2600
0	20.0000	.8089	.2820
0	21.0000	.8063	.3050
0	22.0000	.8189	.3290
0	23.0000	.8408	.3540
0	24.0000	.8668	.3790
0	25.0000	.9023	.4050
0	26.0000	.9406	.4320

35

II

Figure A.1: Experimental data

Table 3. (cont)

0	27.0000	.9912	.4600
0	30.0000	.8550	.5700
0	35.0000	.9800	.7450
0	40.0000	1.0350	.9200
0	45.0000	1.0500	1.0750
0	50.0000	1.0200	1.2150
0	55.0000	.9550	1.3450
0	60.0000	.8750	1.4700
0	65.0000	.7600	1.5750
0	70.0000	.6300	1.6650
0	75.0000	.5000	1.7350
0	80.0000	.3650	1.7800
0	85.0000	.2300	1.8000
0	90.0000	.0900	1.8000
0	95.0000	-.0500	1.7800
0	100.0000	-.1850	1.7500
0	105.0000	-.3200	1.7000
0	110.0000	-.4500	1.6350
0	115.0000	-.5750	1.5550
0	120.0000	-.6700	1.4650
0	125.0000	-.7600	1.3500
0	130.0000	-.8500	1.2250
0	135.0000	-.9300	1.0850
0	140.0000	-.9800	.9250
0	145.0000	-.9000	.7550
0	150.0000	-.7700	.5750
0	155.0000	-.6700	.4200
0	160.0000	-.6350	.3200
0	165.0000	-.6800	.2300
0	170.0000	-.8500	.1400
0	175.0000	-.6600	.0550
1	180.0000	0.0000	.0250
	2000000.0	NACA 0015 SECTION DATA, EPPLER MODEL, -CL, CD, DEC 78	
0	0.0000	0.0000	.0070
0	1.0000	.1100	.0071
0	2.0000	.2200	.0072
0	3.0000	.3300	.0075
0	4.0000	.4400	.0078
0	5.0000	.5500	.0083
0	6.0000	.6600	.0090
0	7.0000	.7700	.0098
0	8.0000	.8800	.0108
0	9.0000	.9574	.0121
0	10.0000	1.0433	.0133
0	11.0000	1.1138	.0146
0	12.0000	1.1667	.0161
0	13.0000	1.1948	.0177
0	14.0000	1.1962	.0195
0	15.0000	1.1744	.0215
0	16.0000	1.1356	.0237

36

Figure A.2: Experimental data

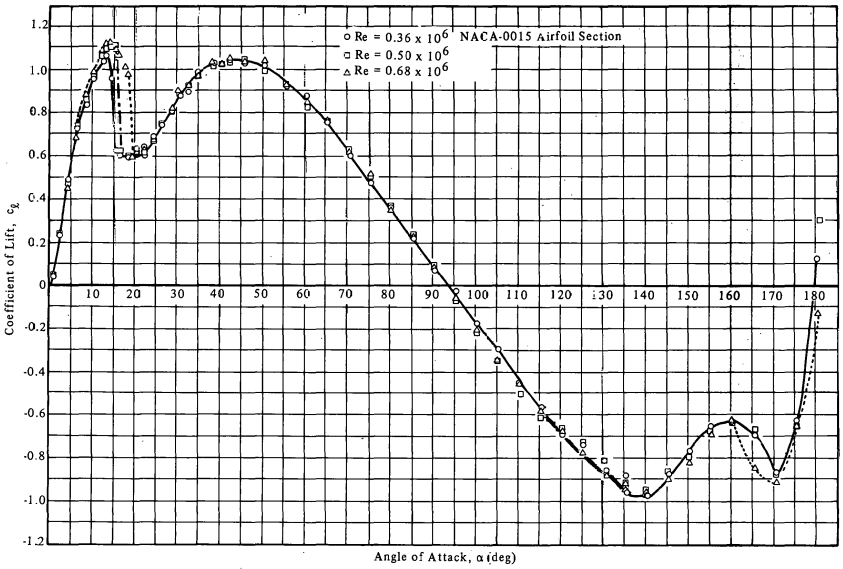

Figure 12. Full Range Section Lift Coefficients for the NACA-0015 Airfoil at Reynolds Numbers of 0.36×10^6, 0.50×10^6, and 0.68×10^6

Figure A.3: Experimental data

DEPARTMENT OF MECHANICS AND MARITIME SCEINCES
CHALMERS UNIVERSITY OF TECHNOLOGY
Gothenburg, Sweden
www.chalmers.se

CHALMERS
UNIVERSITY OF TECHNOLOGY